### A Microphysical Probe of Neutron Star Interiors: Constraining the Equation of State with Glitch Dynamics

ZHONGHAO TU D1 AND ANG LI D1

<sup>1</sup> Department of Astronomy, Xiamen University, Xiamen 361005, China; liang@xmu.edu.cn

### ABSTRACT

Glitches in neutron stars originate from the sudden transfer of angular momentum between superfluid components and the observable crust. By modeling this glitch dynamics—including vortex motion, mutual friction, and angular momentum exchange—we can probe the dense matter equation of state. We match theoretical predictions of glitch rise times, overshoot patterns, and relaxation timescales to the well-documented observations of the 2016 Vela glitch. Our model incorporates microphysical parameters such as the mutual friction coefficient  $\mathcal{B}$ , which in the core arises from electron scattering off magnetized vortices, and in the crust from Kelvin wave excitation during vortex-lattice interactions. Our Markov Chain Monte Carlo analysis of the timing residuals reveals detailed glitch dynamics: the crustal superfluid couples on timescales of  $\sim 100$  seconds, the core exhibits overshoot behavior due to strong central behavior, and the inner crust shows weak entrainment, with  $\sim 70\%$  of free neutrons remaining superfluid. The modeled rise times are consistent with the observed upper limit of 12.6 seconds, and the observed overshoot requires strong crustal friction but weak core friction, supporting a spatially varying  $\mathcal{B}$ . These findings highlight the importance of microphysical modeling and demonstrate the potential of future high-cadence timing observations to further constrain the internal dynamics and composition of neutron stars.

Keywords: Neutron star cores (1107); Neutron stars (1108); Pulsars (1306)

### 1. INTRODUCTION

Pulsars, recognized as the most precise clocks in the universe, display sudden increases in the rotational frequency known as glitches (Reichley & Downs 1969; Radhakrishnan & Manchester 1969; Espinoza et al. 2011; Antonopoulou et al. 2022). These glitches are typically regarded as signatures of superfluidity in stellar interiors (Baym et al. 1969; Anderson & Itoh 1975). The phenomenon occurs when neutron vortices undergo catastrophic unpinning, resulting in rapid angular momentum transfer from the superfluid to the observable crust over a short timescale (Alpar 1977; Haskell & Melatos 2015). The accumulated glitch observations has become a valuable tool for investigating pulsar interiors, yielding insights into their internal structure (Alpar et al. 1993, 1996; Andersson et al. 2012; Watanabe & Pethick 2017; Link 2014; Li et al. 2016; Gügercinoğlu 2017; Gügercinoğlu & Alpar 2020), temperature (Alpar et al. 1984, 1989), the coupling mechanism between superfluid and crust (Sidery & Alpar 2009; Graber et al. 2018; Pizzochero, P. M. et al. 2020; Montoli, A. et al. 2020), and the equation of state (EOS) (Alpar et al. 1993; Hooker et al. 2013; Li & Wang 2017; Yan 2019; Shang & Li 2021; Tu & Li 2025).

Vela (PSR B0833-45) is one of the most frequently glitching pulsars, with 25 observed glitches over the past 56 yr. The sizes and post-glitch recoveries of these glitches have advanced our understanding of the glitch mechanism. Alpar et al. (1993) employed the vortex creep model to analyze post-glitch recoveries from eight of the first nine glitches observed since 1969. They identified three distinct linear response components with short and intermediate time scales, followed by a nonlinear response component. Similar recovery features persist in the four most recent glitches of Vela up to data (Grover et al. 2025). In particular, the sizes of these glitches can be used to constrain the pulsar mass (Pizzochero et al. 2017). The maximum observed glitch of Vela constrains its mass to approximately 1.25-1.45  $M_{\odot}$ . The 2000 Vela glitch exhibited the fastest decay term ( $\sim 1$  minute) to date (Dodson et al. 2002). Hooker et al. (2013) combined the snowplow model to simu-

<sup>&</sup>lt;sup>1</sup> liang@xmu.edu.cn

late the 2000 Vela glitch event, constraining the unclear symmetry energy slope  $L_0$  to below 50 MeV; Tu & Li (2025) further tightened the constraint of  $L_0$  to below 40 MeV by incorporating self-consistent calculations of the crustal pinning forces. Shang & Li (2021) applied the snowplow model to simulate the 2000 Vela glitch using EOSs derived from microscopic Brueckner and relativistic Brueckner theories, suggesting a stiff EOS and a strong suppression of neutron pairing in the crust.

The more recent 2016 Vela glitch, with the fractional change in the pulsar frequency  $\Delta \nu / \nu = 1.431 \times 10^6$ , provided a unique opportunity to study pulse-to-pulse glitch dynamics (Palfreyman et al. 2018). Through several phenomenological models, Ashton et al. (2019) identified unique features, including the overshoot in crustal frequency and rapid relaxation, determining an upper limit of 12.6 s for glitch rise time. These features offer new insights into the coupling dynamics between different internal components in the pulsar interiors. Using density-dependent crustal mutual friction coefficients, Graber et al. (2018) simulated the overshoot and relaxation of the 2016 Vela glitch using a three-component model, suggesting that the glitch rise strongly depends on the relative strength between the crust and core mutual frictions, providing a way to probe both crustal superfluid and deeper interior. Subsequently, Pizzochero, P. M. et al. (2020) investigated the contributions of both the crust and the core to the 2016 Vela glitch, taking into account the entrainment effects. Based on the three-component model, a Bayesian estimation of superfluid moments of inertia from the 2016 Vela glitch was processed in Montoli, A. et al. (2020), the authors confirmed the existence of overshoot and constrained the upper limit of the glitch rise time to approximately 6 s. Additionally, an increase in timing residuals prior to the 2016 Vela glitch was also observed (Palfreyman et al. 2018), which may involve either the slow-down of crustal frequency or magnetospheric changes. The former may involve the formation of vortex traps (Gügercinoğlu & Alpar 2020), and the latter perhaps result from a starquake (Bransgrove et al. 2020).

In this study, we simulate the detailed coupling dynamics within neutron stars (NSs), perform Markov Chain Monte Carlo (MCMC) analyses of the timing residuals of the 2016 Vela glitch to infer key NS pa-

rameters, and establish direct links between microscopic physics and astrophysical observables. The structure of the paper is as follows. Section 2 describes the microphysical inputs adopted in this work. Sections 2.1–2.4 outline the theoretical framework for constructing unified EOSs, the resulting internal composition of NSs, the calculation of pinning energies in the inner crust, and the determination of mutual friction coefficients in both the crust and core. The extended three-component glitch model is introduced in Section 2.5. Theoretical predictions for the glitch rise are presented in Section 3, followed by the evolution of the crustal frequency and corresponding model residuals in Section 3.1. Section 3.2 discusses the effects of the symmetry energy slope  $L_0$ , entrainment, and NS mass on the glitch rise. In Section 4, the three-component model is applied to the 2016 Vela glitch, while Section 4.1 presents the MCMC simulations and parameter inference. A summary of the main conclusions is provided in Section 5.

### 2. MICROPHYSICAL INPUTS

To build a self-consistent glitch model, we require several microphysical inputs: a unified EOS to describe the star's structure, a calculation of neutron superfluidity and vortex pinning energies in the inner crust, and the resulting mutual friction coefficients in both the crust and core. These elements are detailed in the following subsections and subsequently integrated into our three-component dynamical model.

### 2.1. Unified description for the crust and core of neutron stars

Unified EOS demands that all regions of a NS—such as the crust and core—be computed within a single, self-consistent nuclear many-body framework, employing the same underlying nuclear interaction and ensuring consistent composition across different layers (e.g., Fantina et al. 2013). In this study, we consider the nucleons interacting with each other through the exchange of isoscalar scalar and vector mesons ( $\sigma$  and  $\omega$ ), isovector vector meson ( $\rho$ ) in the relativistic mean field (RMF) model (Fetter et al. 1972; Walecka 1974; Serot 1992). The Lagrangian density that describes the systems with time-reversal symmetry can be written as:

$$\mathcal{L} = \sum_{N} \bar{\psi}_{N} \left\{ \gamma^{\mu} \left[ i \partial_{\mu} - g_{\omega N} \omega_{\mu} - g_{\rho N} \boldsymbol{\rho}_{\mu} \boldsymbol{\tau}_{N} - q_{N} A_{\mu} \right] - \left[ M_{N} - g_{\sigma N} \sigma \right] \right\} \psi_{B} 
+ \frac{1}{2} (\partial^{\mu} \sigma \partial_{\mu} \sigma - m_{\sigma}^{2} \sigma^{2}) - \frac{1}{4} W^{\mu \nu} W_{\mu \nu} + \frac{1}{2} m_{\omega}^{2} \omega^{\mu} \omega_{\mu} - \frac{1}{4} \boldsymbol{R}^{\mu \nu} \boldsymbol{R}_{\mu \nu} + \frac{1}{2} m_{\rho}^{2} \boldsymbol{\rho}^{\mu} \boldsymbol{\rho}_{\mu} - \frac{1}{4} A^{\mu \nu} A_{\mu \nu} 
+ \sum_{l=\sigma, \mu} \bar{\psi}_{l} (i \gamma_{\mu} \partial^{\mu} - m_{l} + e \gamma^{0} A_{\mu}) \psi_{l}, \tag{1}$$

where  $\tau_N$  and  $q_N$  are the Pauli matrices and charges of nucleons, and  $M_N$  and  $m_l$  represent the nucleon and lepton masses, respectively.  $g_{mN}$  is the density-dependent coupling constant between the meson m and the nucleon N.  $\psi_{N(l)}$  is the Dirac field of the nucleons or the leptons.  $\sigma$ ,  $\omega_\mu$ , and  $\rho_\mu$  denote the quantum fields of mesons. The field tensors of  $\omega$ ,  $\rho$ , and photon are

$$W_{\mu\nu} = \partial_{\mu}\omega_{\nu} - \partial_{\nu}\omega_{\mu},$$

$$\mathbf{R}_{\mu\nu} = \partial_{\mu}\vec{\rho}_{\nu} - \partial_{\nu}\vec{\rho}_{\mu},$$

$$A_{\mu\nu} = \partial_{\mu}A_{\nu} - \partial_{\nu}A_{\mu}.$$
(2)

The unified EOS within the RMF framework was developed and detailed in our previous studies (e.g., Tu & Li 2025), to which readers are referred for further details. Below, we briefly outline the procedure for constructing such unified EOSs. Compared with nonunified approaches, unified EOSs avoid the artificial introduction of additional degrees of freedom in describing NS properties, thereby providing tighter and more consistent constraints on nuclear theory from astrophysical observations.

Applying the mean-field approximation, the equations of motion of various mesons are obtained via the Euler-Lagrange equation,

$$(-\nabla^2 + m_\sigma^2)\sigma = \sum_N g_{\sigma B} \rho_s^N, \tag{3}$$

$$(-\nabla^2 + m_\omega^2)\omega = \sum_N g_{\omega B} \rho_v^N, \tag{4}$$

$$(-\nabla^2 + m_{\rho}^2)\rho = \sum_{N} g_{\rho B} \rho_v^N \tau_N^3,$$
 (5)

$$-\nabla^2 A_0 = e \left( q_N \sum_N \rho_v^N + q_l \sum_l \rho_v^l \right), \qquad (6)$$

where the meson fields have been replaced by their mean values.  $\rho_v^{N(l)}$  and  $q_{N(l)}$  are the vector density and charge of the nucleon (lepton) species N(l), respectively.  $\rho_s^N$  and  $\tau_N^3$  are the scalar density and isospin projection of the nucleon species N, respectively.

For the core of a NS, the derivative terms in the Eqs. (3)–(6) are eliminated due to the translation invariance of the system. The particle fractions and meson fields can be calculated by iteratively solving the coupled nonlinear system composed of Eqs. (3)–(5), beta equilibrium, charge neutrality, and baryon number conservation conditions. The energy density  $\varepsilon_{\text{core}}$  and pressure  $P_{\text{core}}$  can be derived from the energy-momentum tensor  $\mathcal{T}^{\mu\nu}$  via  $\varepsilon_{\text{core}} = \langle \mathcal{T}^{00} \rangle$  and  $P_{\text{core}} = \langle \mathcal{T}^{kk} \rangle/3$ , respectively.

For the crust of a NS, nuclear matter is nonuniform and the nuclear clusters with different nuclear geometries are immersed in the free neutron sea. Using the Wigner-Seitz and Thomas-Fermi approximations, we obtain the distributions of meson fields and particle densities by iteratively solving the coupled nonlinear system composed of Eqs. (3)–(6), along with the same equilibrium conditions as in the core and the reflective boundary condition, in different cluster geometries. In the outer crust, only spherical nuclei are considered. The nuclear pasta may emerge in the bottom of the inner crust, five representative pasta geometries are conventionally recognized: droplets, rods, slabs, tubes, and bubbles. The microstructure of the inner crust is utilized for semiclassical calculations of the pinning energy and pinning force (as discussed below in the following section). Only droplets are considered in this study due to the current lack of reliable semiclassical methods for vortex pinning on strange pasta structures, i.g., tube, slab, rod, and bubble. After obtaining the density distribution of the WS cell, the droplet size is calculate

$$R_{\rm d} = R_{\rm WS} \left( \frac{\langle \rho_p \rangle^2}{\langle \rho_p^2 \rangle} \right)^{1/3},$$
 (7)

with  $\langle \rho_p \rangle = 4\pi \int_0^{R_{\rm WS}} \rho_p r^2 {\rm d}r/V$  and  $\langle \rho_p^2 \rangle = 4\pi \int_0^{R_{\rm WS}} \rho_p^2 r^2 {\rm d}r/V$ .  $\rho_p = \rho_v^p$  is the vector density of protons. r is the radial distance.  $R_{\rm WS}$  and V are the radius and volume of WS cell, respectively. The energy density  $\varepsilon_{\rm crust}$  is obtained by integrating the energy density functional for the internal structure of the crust and then the pressure is evaluated using the thermodynamic relation,  $P_{\rm crust} = \sum_{i=n,p,e} \mu_i \rho_v^i - \varepsilon_{\rm crust}$ , with the chemical potentials of nucleons and electrons  $\mu_i$ .

Table 1. Nuclear matter saturation properties for the DD-ME2 and PKDD effective interactions. Listed are the saturation density  $\rho_0$  (fm<sup>-3</sup>), binding energy per particle E/A (MeV), incompressibility  $K_0$  (MeV), skewness  $Q_0$  (MeV), symmetry energy  $J_0$  (MeV), slope of symmetry energy  $L_0$  (MeV), and effective mass of neutron  $M_n^*/M_n$ .

	$\rho_0$	E/A	$K_0$	$Q_0$	$J_0$	$L_0$	$M_n^{\star}/M_n$
	${\rm fm}^{-3}$	MeV	${ m MeV}$	${ m MeV}$	${\rm MeV}$	${ m MeV}$	
DD-ME2	0.152	-16.14	251.1	479	32.30	51.26	0.572
PKDD	0.150	-16.27	262.2	-115	36.86	90.21	0.570

In this work, we construct the unified EOS using two sets of density-dependent effective interaction: DD-ME2 (Lalazissis et al. 2005) and PKDD (Long et al. 2004). The original DD-ME2 and PKDD demonstrate support for the existence of massive NSs ( $> 2M_{\odot}$ ). The extension of DD-ME and PKDD in the isospin vector channel can be obtained by adjusting the density-dependent coupling parameters, i.e.,  $g_{\rho}$  and  $a_{\rho}$ , for the  $\rho$  meson;

Table 2. Coupling parameters  $g_{\rho}$  and  $a_{\rho}$  between nucleons and  $\rho$  meson, transition densities of NS matter, and maximum mass NS  $M_{\rm TOV}$  for the DD-ME2 and PKDD interactions, adjusted to different values of the symmetry energy slope  $L_0$ . The transition densities of NS matter include  $\rho_{\rm oi}$  between the outer and inner crusts and  $\rho_{\rm cc}$  between the crust and core.

	DD-ME2				PKDD			
$L_0 \text{ (MeV)}$	30	40	60	80	30	40	60	80
$g_{ ho}$	3.357	3.528	3.792	4.010	3.629	3.769	4.006	4.206
$a_{ ho}$	0.891	0.721	0.460	0.258	0.827	0.684	0.453	0.267
$\rho_{\rm oi} \ (10^{-4} \ {\rm fm}^{-3})$	1.902	1.944	2.035	2.129	1.416	1.431	1.463	1.496
$\rho_{\rm cc}~({\rm fm}^{-3})$	0.095	0.085	0.067	0.055	0.097	0.087	0.075	0.067
$M_{ m TOV}~(M_{\odot})$	2.497	2.491	2.477	2.468	2.356	2.350	2.336	2.325

see (Tu & Li 2025) for details. In Table 1, we list the saturation properties of nuclear matter for the original effective interactions. The coupling parameters of extensions of two effective interactions are listed in Table 2 with  $L_0=30,\ 40,\ 60,\$ and 80 MeV. These coupling parameters are obtained by fixing the symmetry energy  $E_{\rm sym}$  at  $\rho_{\rm B}=0.11\ {\rm fm^{-3}}$  but adjusting the symmetry energy slope  $L_0$  at the saturation density. For unified EOS, the transition density  $\rho_{\rm oi}$  between the outer crust and inner crust, and  $\rho_{\rm cc}$  between the crust and core are also affected by effective interaction both in the isospin scalar and vector channels, see Table 2.

### 2.2. Superfluidity and pinning energy

Prior to calculating the pinning energy and pinning force in the inner crust, we need to derive the neutron pairing gap within the inner crust. Based on the local density approximation (LDA), the neutron pairing gap is solved through the standard Bardeen–Cooper–Schrieffer (BCS) approximation

$$1 = -\frac{1}{4\pi^2} \int k^2 dk \frac{G_N p^2(k)}{\sqrt{[E_N(k) - \mu]^2 + \Delta_0^2 p^2(k)}}, \quad (8)$$

phenomenological pairing  $V_{\text{pair}}(k, k') = G_N p(k) p(k')$  with  $p(k) = \exp(-\alpha^2 k^2)$ is adopted,  $G_N = 738 \text{ MeV} \cdot \text{fm}^3$  is the pairing strength between nucleons and  $\alpha = 0.636$  fm is finite range, following (Tian et al. 2009). E(k) is the neutron single particle energy obtained by DDRMF model, the chemical potential  $\mu_n$  is determined by the value of E(k)at the Fermi surface, i.e.,  $\mu_n = E(k_{\rm F})$  with the Fermi momentum  $k_{\rm F}$ .  $\Delta(k) = \Delta_0 p(k)$  is the trivial solution of the Eq. (8) and we mainly refer the neutron pairing gap at the Fermi surface  $\Delta_n \equiv \Delta_0 p(k_{\rm F})$ . We incorporate a scaling factor to account for the suppression of the pairing gap by medium polarization, expressed as  $\Delta_n(\beta) = \Delta_n/\beta$ . Our previous studies (Shang & Li 2021; Tu & Li 2025), which modeled the 2000 Vela glitch using the snowplow framework, demonstrated a strong polarization effect. Following these results, we adopt  $\beta = 3.0$  in this work.

The semiclassical method for calculating pinning energy in the relativistic case has been developed. We provide a brief introduction below, and the interested reader can refer to Tu & Li (2025) for further details. We calculate the pinning energy as the difference of energy cost  $E_{\rm cost}$  between two typical pinning configurations: the pinning of vortices on nuclei surrounded by the neutron sea (NP configuration) and the pinning of vortices in the neutron sea between two adjacent nuclei (IP configuration). We establish a cylindrical container with radius  $R_{\rm WS}$  and height  $2R_{\rm WS}$ . When placing a nucleus at the center of container and filling the remaining space with free neutrons, then creating a neutron vortex coaxial with the cylinder axis, we obtain the NP configuration, corresponding to the local energy cost  $E_{\text{cost}}^{\text{NP}}$  of vortex creating. If we fill the container solely with free neutrons and creating a coaxial neutron vortex, the IP configuration with its corresponding local energy cost  $E_{
m cost}^{
m IP}$  is obtained. Consequently, the pinning energy is given by

$$E_{\rm p} = 2\pi \int_0^{2R_{\rm ws}} \int_0^{R_{\rm ws}} \left( E_{\rm cost}^{\rm IP} - E_{\rm cost}^{\rm NP} \right) \rho \mathrm{d}\rho \mathrm{d}z, \quad (9)$$

where polar coordinate is employed. The kinetic energy per unit volume

$$E_{\rm kin} = \frac{\hbar^2 \rho_n}{8M^* r^2},\tag{10}$$

and condensation energy per unit volume

$$E_{\rm cond} = -\frac{3\Delta_n^2 \rho_n}{8e_n},\tag{11}$$

of the vortex contribute to the local energy cost. r is the distance of a point within the vortex to the vortex axis.  $\rho_n$  is the local density of the neutron with in the WS cell.  $e_n = \sqrt{k_{\mathrm{F},n}^2 + M_n^{\star 2}} - M_n^{\star}$  is the Fermi energy which subtract the (in-medium) rest mass with Fermi momentum  $k_{\mathrm{F},n}$  of neutrons. If the kinetic energy exceeds the

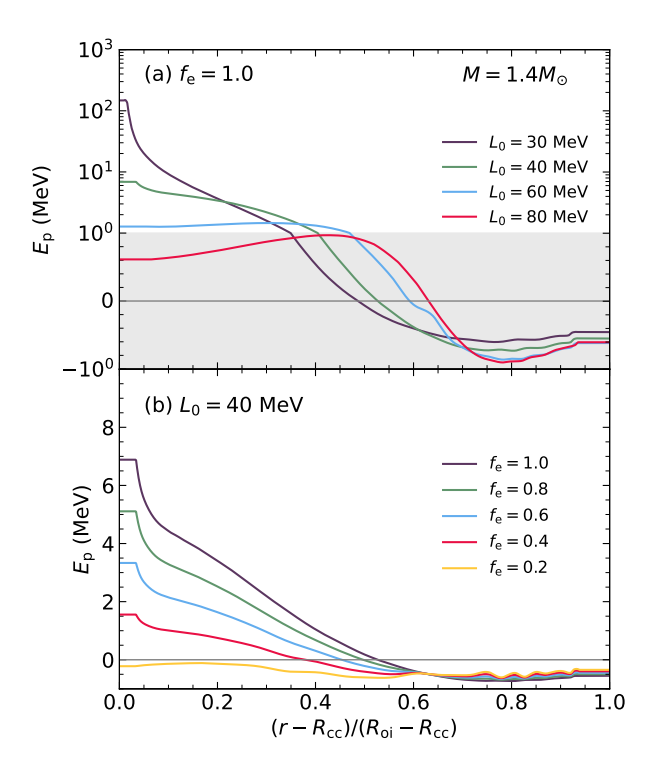


Figure 1. Radial profiles of pinning energy  $E_{\rm p}$  in the inner crust of a  $1.4 M_{\odot}$  neutron star. (a) Dependence on the symmetry energy slope  $L_0$  for the PKDD interaction, with no entrainment ( $f_{\rm e}=1.0$ ). The gray shaded region uses a linear scale for  $-1 < E_{\rm p} < 1$  MeV. (b) Dependence on the entrainment factor  $f_{\rm e}$  for PKDD with  $L_0=40$  MeV. Stronger entrainment (lower  $f_{\rm e}$ ) significantly suppresses pinning energy in the bottom of the crust.

condensation energy of superfluid neutrons, the neutron Cooper pairs are destroyed, causing the transition of superfluid neutrons to normal neutrons. Then the local energy cost is written as follows

$$E_{\text{cost}} = \begin{cases} \frac{\hbar^2 \rho_n}{8M_n^* r^2}, \ r > R_t(z) \\ \frac{3\Delta_n^2 \rho_n}{8e_n}, \ r \le R_t(z), \end{cases}$$
(12)

where the transition radius  $R_t(z)$  is determined by the balance of Eqs. (10) and (11). The coherence length  $\xi$  is widely used to represent the vortex core size,

$$\xi = \frac{k_{\mathrm{F},\infty}}{\pi M_{\infty}^* \Delta_{\infty}},\tag{13}$$

where  $k_{F,\infty}$ ,  $M_{\infty}^*$ , and  $\Delta_{\infty}$  are the Fermi momentum, effective mass, and pairing gap of free neutrons, respectively.

In the above, we assume all free neutrons in the inner crust are superfluid  $\rho_s = \rho_n^{\infty}$ ,  $\rho_n^{\infty}$  is the baryon density of free neutrons. However, the entrainment effect causes a part of free neutrons to flow with the nuclei,

resulting in a reduction of the superfluid density. The extent to which the entrainment effect suppresses the superfluid density remains still debated (Oyamatsu & Yamada 1994; Carter et al. 2005; Chamel 2005; Kashiwaba & Nakatsukasa 2019). By carrying out the full band structure calculations of free neutrons in bodycentered cubic lattices, Chamel (2024) found a strong entrainment effect at a density of 0.03 fm<sup>-3</sup> in the inner crust, only 8% of free neutrons participating in the superflow. In contrast, Almirante & Urban (2025), using the linear response theory, found approximately 90% of free neutrons to be effectively superfluid. To account for entrainment effects in our study, we introduce a global scaling factor  $f_{\rm e}$ , i.e., the fraction of free neutrons participating in superflow, for all density ranges of the inner crust. Note that the introduction of  $f_{\rm e}$  is a simplified approximation, for instance, it does not account for the influence of the density of the inner crust or pairing gap on the entrainment effects. Since  $f_{\rm e}$  does not alter the single-particle properties of free neutrons, the Fermi momentum, effective mass, and pairing gap of superfluid neutrons, as well as the coherence length of vortex, remain unchanged. However, due to  $\rho_s = f_e \rho_n^{\infty}$ , both the pinning energy and pinning configurations could be modified.

Tu & Li (2025) has discussed how  $L_0$  affects the density dependence of the pinning energy in detail. To maintain consistency with the coupled dynamics introduced later, here we first transform the density dependence of the pinning energy into a radial profile, i.e., the pinning energy as a function of normalized radial distance  $(r - R_{cc})/(R_{oi} - R_{cc})$  in the inner crust, for a NS of a given mass by solving the Tolman-Oppenheimer-Volkoff (TOV) equations, and then we revisit the effect of  $L_0$  on the radial profile of pinning energy. Here r is the radial distance from a point r to the center of the NSs, and  $R_{\rm cc}$  and  $R_{\rm oi}$  are the radial distances corresponding to densities  $\rho_{\rm cc}$  and  $\rho_{\rm oi}$  in an NS with a given mass. In Figure 1(a), we present the radial profiles of the pinning energy in the inner crust, using PKDD with different  $L_0$ values as examples. For this comparison, we fix  $f_{\rm e} = 1.0$ and the NS mass at 1.4  $M_{\odot}$ . The vortex pinning transition from IP to NP configuration occurs in the middle region of the inner crust at  $(r - R_{\rm cc})/(R_{\rm oi} - R_{\rm cc}) \sim 0.5$ 0.7, corresponding to the density range 0.01-0.02 fm<sup>-3</sup>. In the top of the inner crust, the vortices prefer the IP configuration, where the pinning strength increases with  $L_0$ , but  $|E_p|$  is always below 1 MeV; in the bottom of the inner crust, the vortices prefer the NP configuration, with  $E_{\rm p}$  increasing as  $L_0$  decreases, accompanied by the peak of pinning energy gradually moving toward the crust-core interface and disappearing at  $L_0 \leqslant 40$  MeV. Here we calculate  $E_{\rm p}$  only at some discrete densities, and we apply a spline function to interpolate  $E_{\rm p}$  between the maximum and minimum densities. For densities outside this range or in the corresponding inner crust regions, we keep  $E_{\rm p}$  constant for simplicity.

Figure 1(b) demonstrates the influence of the entrainment effect on the radial profile of the pinning energy in the inner crust. We observe that in the top of the inner crust, the enhancement of the entrainment effect, i.e., the reduction of  $f_e$ , slightly weakens the pinning strength; however, in the bottom of the inner crust, the entrainment effect significantly reduces the pinning energy. The latter can be explained by Eq. (9). We have assumed that the entrainment effect does not alter the single-particle properties of neutrons, and hence the transition radius  $R_t(z)$  of the vortex remains unchanged. In the NP configuration,  $R_t(z)$  essentially envelopes the nuclei; therefore, the dominant contribution in Eq. (9) stems from the difference of condensation energy  $E_{\rm cond}$  in the vortex core between the two configurations. For the IP configuration,  $E_{\rm cond}^{\rm IP} \propto f_{\rm e}$ ; for the NP configuration,  $E_{\rm cond}^{\rm IP}$  mainly involves the region containing nuclei,  $E_{\rm cond}^{\rm IP}$  decreases slightly with reducing  $f_{\rm e}$ . As a result, the pinning energy  $E_{\rm p}$  decreases significantly with decreasing  $f_{\rm e}$ , and the IP configuration can even become fully favored when  $f_{\rm e} < 0.4$ . Accordingly, as  $f_{\rm e}$  decreases, the transition point between pinning configurations shifts toward the crust-core boundary and disappears altogether for  $f_e < 0.4$ .

Moreover, the influence of NS mass on the pinning energy profile is found to be negligible. In addition, the results obtained with DD-ME2 are qualitatively consistent with those from PKDD.

## 2.3. Kelvin wave excitation and mutual friction in the inner crust

The vortex is pinned to the top of the nuclei or the neutron sea between two adjacent nuclei in the inner crust because of its interaction with the nuclei. The large-scale unpinning of vortices leads to the transfer of angular momentum from the superfluid component to the normal component, triggering a glitch. During a glitch, there exists a local velocity  $\Delta v$  between a vortex and a nucleus, then the dynamics of vortex is fully characterized by a dimensionless drag parameter  $\mathcal R$  and the vortex feels a resistive per unit length

$$f_{\rm res} = \rho_{\rm s} \kappa \mathcal{R} \Delta v,$$
 (14)

where  $\rho_s$  is the mass density of superfluid neutron,  $\kappa$  is quantum of circulation with a approximate value  $2.0 \times 10^{-3} \text{ cm}^2 \text{ s}^{-1}$ . Assuming that a large number of vortices moves freely and experiences  $f_{\text{res}}$ , the micro-

scopic drag is related to the large-scale hydrodynamic mutual friction coefficient  $\mathcal{B}$  (Glampedakis et al. 2011)

$$\mathcal{B} = \frac{\mathcal{R}}{1 + \mathcal{R}^2}.\tag{15}$$

In this study, we discuss Kelvin wave dynamics based on the work of Epstein & Baym (1992). When a vortex passes through a lattice nucleus, their interaction  $f \sim \delta(z) E_{\rm p}/\ell$  (with a duration of  $\tau \sim \ell/\Delta v$ ) excites Kelvin wave with characteristic frequencies  $\omega \lesssim \tau^{-1}$ , wavenumber  $k \lesssim k_\star \equiv (2\mu/\hbar\tau)^{1/2}$ , and the Fourier-transformed amplitude  $\bar{\epsilon}(k \lesssim k_\star) \sim E_{\rm p}\tau/\rho_{\rm s}\kappa l$ . Here  $E_{\rm p}$  and l are the pinning energy and typical interaction scale, respectively.  $\mu$  is the effective mass of the neutrons associated with the vortex tension, we follow Graber et al. (2018) and set  $\mu \approx M_n/2$ .  $\hbar$  is the reduced Planck constant. Then the energy dissipation is estimated by

$$\Delta E \sim \int T k^2 \tilde{\epsilon} (k)^2 dk \sim \frac{\hbar k_*^3}{\rho_s \kappa \mu} \left(\frac{E_p}{\Delta v}\right)^2,$$
 (16)

where  $T = \rho_s \kappa \hbar/2\mu$  is the vortex tension. Based on the work of Epstein & Baym (1992), the power transferred to Kelvin waves per unit length is obtained by

$$p \sim n_1 \Delta v \int \Delta E(b) db \sim \frac{\hbar k_*^3}{\rho_s \kappa \mu} \left(\frac{E_p}{\Delta v}\right)^2 n_1 \ell \Delta v,$$
 (17)

where  $n_{\rm l}$  and b are the number density of nuclei and impact parameter, respectively. The resistive force can be calculated by power,  $f_{\rm res} = p/\Delta v$ . Combining Eq. (14) and  $k_{\star}$ , we get

$$\mathcal{R}_{\rm EB} \simeq 1.4 \left(\frac{\mu}{\hbar}\right)^{1/2} \left(\frac{E_{\rm p}}{\rho_{\rm s}\kappa}\right)^2 \frac{1}{\Delta v^{3/2}} \frac{n_{\rm l}}{R_{\rm d}^{1/2}},$$
 (18)

where we have assumed that potential falls off on the scale of the nuclear radius, i.e.,  $\ell \simeq R_{\rm d}$ .

The local velocity lag  $\Delta v$  is typically of the same order as the critical lag  $\Delta \omega_{\rm cr} = \Delta v_{\rm cr} r$  and we estimate

$$\Delta v \simeq \Delta v_{\rm cr} = \frac{f_{\rm pin}}{\rho_s \kappa}.$$
 (19)

We have calculated the microscopic structure of the inner crust and pinning properties of vortex in the case of sphere nuclei. The bcc lattice constant a is related to the WS cell size  $R_{\rm WS}$ ,  $a=4R_{\rm WS}/\sqrt{3}$ . The number density of nuclei is  $n_{\rm l}=1/V_{\rm WS}$ , where  $V_{\rm WS}=4\pi R_{\rm ws}^3/3$  is the volume of WS cell. The pinning force per unit length  $f_{\rm pin}$  can be estimated by the method developed in Seveso et al. (2016). An extra parameter presented in the calculation is the vortex rigidity length l. Previous work

Table 3. Comparison of Friction Mechanisms in Neutron Stars.

Mechanism	Assumptions	Observational Signatures	Parameters and Ranges
Crust: Kelvin Wave Excitation	Rigid vortices ( $l \approx 5000R_{\rm ws}$ ); Semiclassical $E_{\rm p}$ calculation; BCC nuclear lattice; Global entrainment effect.	Rise time < 12.6 s (Vela); Crustal frequency overshoot (if relatively weak core fric- tion); Complex relaxation profile	Mutual friction coefficient $\mathcal{B}_{\text{crust}} \sim 10^{-4} \text{ to } 10^{-1}$ ; Pinning energy $E_{\text{p}} \sim -1 \text{ to } +10$ MeV (> 100 MeV for $L_0 = 30$ MeV); Entrainment factor $f_e$ : 0.05-1.0 (0.7 median); Symmetry energy slope $L_0$ : 30-80 MeV.
Core: Electron Scattering	Proton superconductivity; Magnetized vortices; Weak coupling regime.	Overshoot decay time ~100 s; Core superfluid frequency overshoot; Long-term momentum transfer.	Mutual friction coefficient $\mathcal{B}_{\text{core}} \sim 10^{-5} \text{ to } 10^{-4};$ Effective mass ratio $\mathcal{M}_p^*/\mathcal{M}_p$ : 0.5–0.7; Proton fraction $Y_p \sim 0.05$ –0.1, core density $\rho \sim 10^{14} \text{ g/cm}^3$ .
Core: Vortex-Fluxtube Pinning (Alternative)	Type-II superconductor; Strong vortex-fluxtube in- teraction; Magnetic interaction domi- nates.	Stronger core-"crust" coupling; Alters rise/overshoot (not observed).	$\mathcal{B}_{\rm core} \sim 10^{-2}$ (if dominant); Pinning energy $E_{\rm p} \sim 5$ MeV; Magnetic field $B \sim 10^{12}$ G, London penetration depth $\lambda \sim 100$ fm.

### Key Conclusions of the present analysis:

- Observed  $\mathcal{B}_{\text{core}} \sim 10^{-4}$  supports electron scattering, rules out vortex-fluxtube pinning.
- Overshoot of crustal frequency observed in Vela requires strong  $\mathcal{B}_{\text{crust}}$  and weak  $\mathcal{B}_{\text{core}}$ , consistent with Graber et al. (2018).
- $f_e \sim 0.7$  suggests a weak entrainment effect.
- Symmetry energy slope  $L_0$  affects glitch rise and overshoot decay of crustal frequency.

has shown that the vortex rigidity length l is enough long ( $l > 2500R_{\rm ws}$ ), equivalently, the vortex tension is strong (Tu & Li 2025). We choose  $l = 5000R_{\rm ws}$  in our estimation. The pinning force is effectively suppressed after considering the effects of displacement of nuclei in the presence of vortex pinning as well as polycrystalline structure of the lattice in the case of different orientations with respect to the vortices. To ensure consistency between the pinning energy  $E_{\rm p}$  and the critical velocity lag  $\Delta v$  in Eq. (18), we adopt an effective pinning energy  $E_{\rm p}\delta$  which is defined by the relation  $f_{\rm pin} = E_{\rm p}\delta/la$ , where the dimensionless parameter  $\delta$  is calibrated from our calculated values of  $E_{\rm p}$  and  $f_{\rm pin}$ . Finally, the drag parameter is expressed as

$$\mathcal{R}_{\rm EB} \simeq 1.4 \left(\frac{\mu}{\hbar}\right)^{1/2} \left(\frac{E_{\rm p}\delta}{\rho_{\rm s}\kappa}\right)^{1/2} \frac{R_{\rm d}}{a^{3/2}},\tag{20}$$

We derive the radial profiles of the mutual friction coefficients  $\mathcal{B}_{\text{crust}}$  in the inner crust from Figure 1 by using Eq. (20), as we can see in Figure 2. Due to the transition of the pinning configurations,  $E_{\text{p}}$  can cross the

zero point, at which point according to Eq. (20),  $\mathcal{B}_{\text{crust}}$ equals zero. Consequently, a deep valley appears near the configuration transition point. In the realistic crust of NSs, vortices may pin to lattice defects. Assuming a low impurity parameter  $Q_{\text{imp}}$  in the inner crust, there exists a baseline  $\mathcal{B}_{crust}$  in the inner crust, we simply set it to  $1 \times 10^{-4}$ . This setting also prevents numerical errors when solving the three-component glitch model introduced later.  $\mathcal{B}_{\text{crust}}$  falls within the range of  $1 \times 10^{-4}$  to  $1 \times 10^{-1}$ . Approaching the top of the inner crust,  $\mathcal{B}_{\text{crust}}$ increases from  $1 \times 10^{-3}$  to  $1 \times 10^{-2}$ ; in other regions of the inner crust, except near the deep valley,  $\mathcal{B}_{\text{crust}}$  remains on the order of  $1 \times 10^{-3}$ . This indicates that the top of the inner crust is a strong coupling region, while the deep valley is a weak coupling region, reflecting the complicated density dependence in the coupling dynamics. From the inner-outer crust interface to the crustcore interface, neutrons gradually drip out of nuclei to form superfluid neutrons. Since the superfluid density increases with crustal depth (or increasing baryon density, see Figure 1(d) of Tu et al. (2025)), the region near

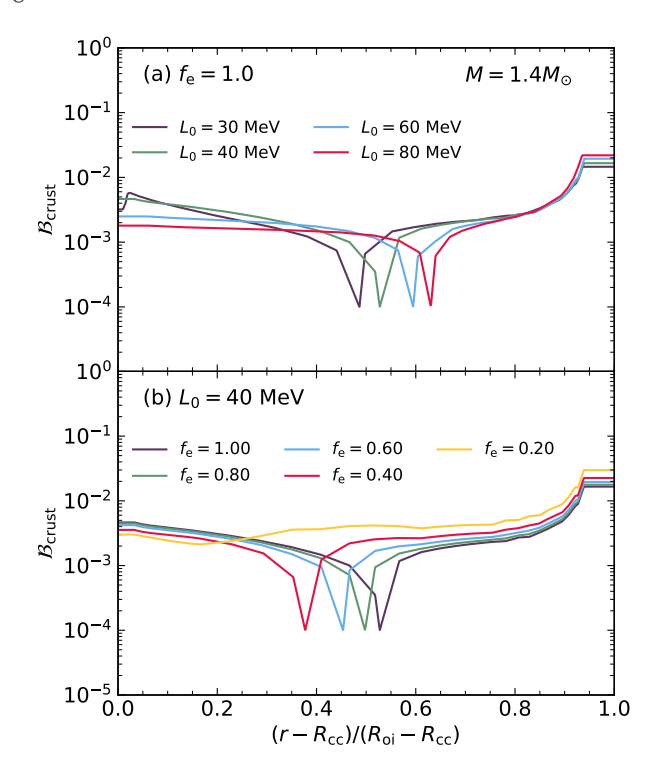


Figure 2. Radial profiles of mutual friction coefficients  $\mathcal{B}_{crust}$ , which derived from Fig. 1 with unchanged settings, in the inner crust.

the crust-core interface carries majority of the superfluid's mass. This results in the strongly coupling region in the top of the inner crust contributing little to angular momentum transfer during a glitch.

The entrainment effect and  $L_0$  appear unable to cause order of magnitude changes in  $\mathcal{B}_{crust}$ , but significantly affect its distribution within the inner crust. As  $L_0$  increases, weakly coupling region shifts toward the innerouter crust interface and contributes less to the glitches. Stronger entrainment effects shift the weak coupling region toward the crust-core interface. However, if the entrainment effect is sufficiently strong ( $f_e < 0.4$ ), vortices uniformly favor the IP configuration, eliminating both configuration transition and weak coupling region. Mutual friction coefficient in the bottom of the inner crust plays a more important role in glitch rises. As we can see from Figure 2(a),  $\mathcal{B}_{\text{crust}}$  in this region increases with decreasing  $L_0$ , consistent with the correlation between pinning energy and  $L_0$ . However, when  $L_0$  decreases to 30 MeV,  $\mathcal{B}_{crust}$  becomes non-monotonic in this region. This behavior originates from the suppression of mesoscopic pinning forces by the extremely dense inhomogeneous structure in the bottom of the inner crust, leading to the reduction of  $\delta$  in Eq. (20). From Figure 2(b), we see that the entrainment effect leads to a monotonic reduction of the mutual friction coefficient in this region, indicating that stronger entrainment more effectively suppresses the angular momentum transfer rate during glitch rise. The results obtained with DD-ME2 show qualitatively the same trend.

### 2.4. Mutual friction in the core

In the core, we focus mainly on the vortex dynamics which is dominated by the scattering of electrons off magnetized vortices. The mutual friction coefficient reads (Andersson et al. 2006)

$$\mathcal{B}_{\text{core}} \simeq 4 \times 10^{-4} \left(\frac{\delta \mathcal{M}_p^*}{\mathcal{M}_p}\right)^2 \left(\frac{\mathcal{M}_p}{\mathcal{M}_p^*}\right)^{1/2} \left(\frac{Y_p}{0.05}\right)^{7/6} \left(\frac{\rho}{10^{14} \text{ g/cm}^3}\right)^{1/6},$$
 (21)

where  $\mathcal{M}_p = M_p$  is the bare proton mass, while  $\mathcal{M}_p^*$  is the effective proton mass associated with the entrainment effect.  $\delta \mathcal{M}_p^* = \mathcal{M}_p - \mathcal{M}_p^*$ .  $Y_p$  is the proton fraction and  $\rho$  is the mass density in the unit of  $g/cm^3$ . To fall within the weak coupling regime, an effective proton mass  $\mathcal{M}_p^*/\mathcal{M}_p = 0.5$ –0.7 is recommended. In Figure 3, we show the mutual friction coefficients  $\mathcal{B}_{core}$  as a function of the normalized radial distance  $r/R_{cc}$  in the core. We can see that  $\mathcal{B}_{core}$  exhibits monotonic growth toward the NS center before reaching a plateau, with its magnitude extending from  $10^{-5}$  to  $10^{-4}$ . A smaller effective mass, or a stronger entrainment effect, leads to a larger  $\mathcal{B}_{core}$ . Near the crust-core interface,  $\mathcal{B}_{core}$  is inversely

correlated with  $L_0$ , which means that it increases as  $L_0$  increases; however, in the center of the NSs, the opposite trend holds.

An alternative, stronger source of mutual friction in the core may originate from the pinning of neutron vortices to fluxtubes, provided that core protons form a type II superconductor. Considering that the vortex-fluxtube interaction is predominantly magnetic, the pinning energy is estimated to be about 5 MeV with the London penetration depth  $\sim 100$  fm (Link 2003; Graber et al. 2017). Assuming a fiducial magnetic field strength of  $\sim 10^{12}$  G and a local relative vortex–fluxtube veloc-

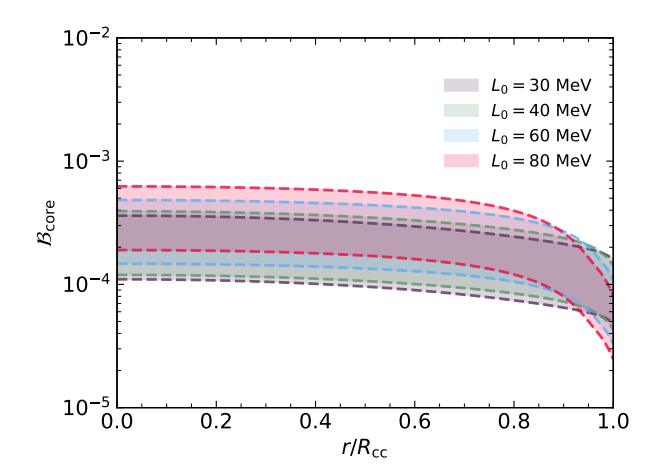


Figure 3. Mutual friction coefficients  $\mathcal{B}_{\text{core}}$  as a function of normalized radial distance  $r/R_{\text{cc}}$  in the core for PKDD with different  $L_0$  and fixed  $1.4M_{\odot}$  NS mass. The shaded region indicates the range of  $\mathcal{B}_{\text{core}}$  for  $\mathcal{M}_p^*/\mathcal{M}_p = 0.5$ –0.7, with the upper and lower boundaries corresponding to  $\mathcal{M}_p^*/\mathcal{M}_p = 0.5$  and  $\mathcal{M}_p^*/\mathcal{M}_p = 0.7$ , respectively.

ity of  $\Delta v \approx 4 \times 10^4$  cm/s, we estimate  $\mathcal{B}_{\rm core} \sim 10^{-2}$ , following the same procedure outlined in Section 2.3.

The stark contrast between these two mechanisms is summarized in Table 3. The orders-of-magnitude difference in  $\mathcal{B}_{\text{core}}$  provides a clear discriminant. As our subsequent MCMC analysis in Section 4.2 will show, the observed glitch dynamics of Vela are consistent only with the weaker friction from electron scattering, effectively ruling out vortex-flux-tube pinning as the dominant coupling mechanism in this pulsar's core.

Eq. (21) indicates that the core mutual friction coefficient  $\mathcal{B}_{\text{core}}$  is density-dependent. To illustrate the resulting differential rotation within the core, we employed Eq. (21) in Section 3. By contrast, in Section 4, a global  $\mathcal{B}_{\text{core}}$  is adopted to examine the overall magnitude of core friction and its role in glitch dynamics.

### 2.5. Three-component glitch model

We extend the three-component glitch model based on Graber et al. (2018) and Haskell & Melatos (2015) to further consider the differential rotation of the core superfluid, which arises from the density-dependent of  $\mathcal{B}_{core}$ . The three components are the crust superfluid, the core superfluid, and the "crust"; the "crust" component represents the solid crust and all components tightly coupled to solid crust. If we neglect the possible external spin-down torque and magnetospheric change, the angular momentum exchange between the three components—the crustal superfluid, the core superfluid, and the collectively coupled "crust"—is governed by the fol-

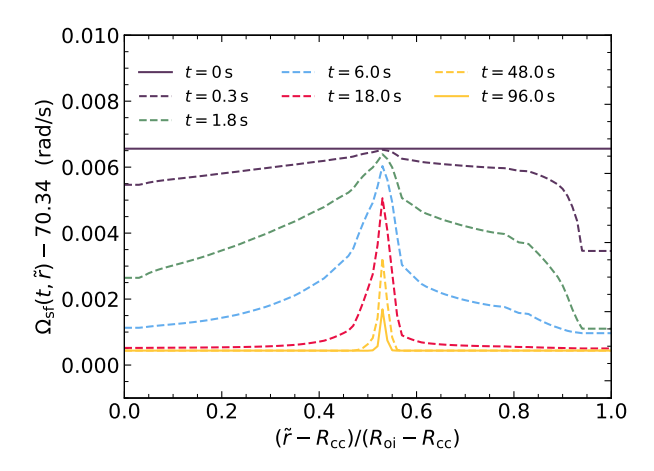


Figure 4. Crustal superfluid angular velocity  $(\Omega_{\rm sf})$  as a function of the normalized crust radial distance  $(\tilde{r}-R_{\rm cc})/(R_{\rm oi}-R_{\rm cc})$  and time t following a glitch. The results are calculated with PKDD with  $L_0=40$  MeV. The entrainment  $f_{\rm e}=1.0$  and NS mass  $1.4M_{\odot}$  are adopted.

lowing set of equations:

$$\dot{\Omega}_{\rm sf} = \mathcal{B}_{\rm crust} \left[ 2\Omega_{\rm sf} + \tilde{r} \frac{\partial \Omega_{\rm sf}}{\partial \tilde{r}} \right] (\Omega_{\rm crust} - \Omega_{\rm sf}), (22)$$

$$\dot{\Omega}_{\rm core} = \mathcal{B}_{\rm core} \left[ 2\Omega_{\rm core} + \tilde{r} \frac{\partial \Omega_{\rm core}}{\partial \tilde{r}} \right] (\Omega_{\rm crust} - \Omega_{\rm core}), (23)$$

$$\dot{\Omega}_{\rm crust} = -\frac{\int \rho_s \tilde{r}^2 \dot{\Omega}_{\rm core} \, dV}{I_{\rm crust}} - \frac{\int \rho_s \tilde{r}^2 \dot{\Omega}_{\rm sf} \, dV}{I_{\rm crust}} (24)$$

where  $\Omega_{\rm sf}$ ,  $\Omega_{\rm core}$ , and  $\Omega_{\rm crust}$  are the angular velocities of the crust superfluid, core superfluid, and "crust" components, respectively.  $I_{\text{crust}}$  is the moment of inertia of "crust" component. The differential rotation between the core and crust superfluids implies that  $\Omega_{\rm sf}$  and  $\Omega_{\rm core}$ evolve as time and space. Following the treatment of Graber et al. (2018), the cylindrical geometry is used, and the cylindrical plane adopts the geometric structure of the equatorial plane of the stellar. We rescale the stellar by matching the total moment of inertia of the cylindrical star to that of a spherical star. The initial conditions for solving Eqs. (22)–(24) are taken from the typical values of Vela, i.e.,  $\Omega_{\rm crust}(t=0) \approx$  $\Omega_{\rm core}(t=0) \approx 70.34026 \text{ rad/s } (\nu \approx 11.195 \text{ Hz}) \text{ and}$  $\Omega_{\rm sf}(t=0) - \Omega_{\rm crust}(t=0) \approx 6.3 \times 10^{-3} \text{ rad/s (Pal$ freyman et al. 2018; Graber et al. 2018). We take the boundary conditions  $\dot{\Omega}_{\rm sf} = \dot{\Omega}_{\rm core} = 0$  at  $\tilde{r} = 0$  and  $\tilde{r} = R$ , where R is the NS radius.

In Figures 4 and 5, we show the spatial and temporal evolutions of  $\Omega_{\rm sf}$  and  $\Omega_{\rm core}$  of  $1.4 M_{\odot}$  NS. The effective interaction PKDD with  $L_0=40$  MeV is adopted and there is no entrainment effect ( $f_{\rm e}=1.0$ ).

In Figure 4, the differential rotation and coupling of the crustal superfluid are visualized, which shows the spatial and temporal evolution of its angular velocity,

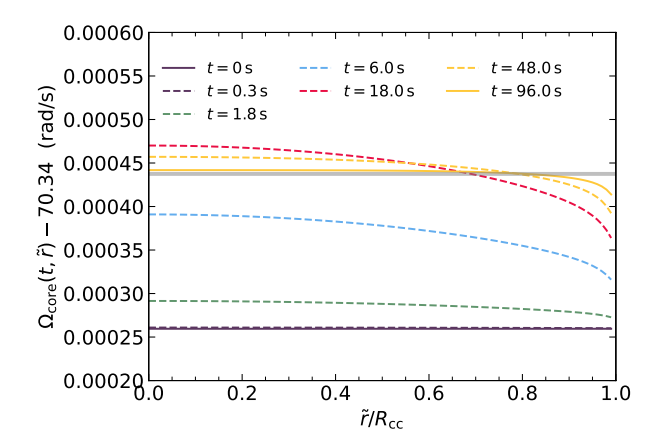


Figure 5. Core superfluid angular velocity ( $\Omega_{\rm core}$ ) as a function of the normalized crust radial distance  $\tilde{r}/R_{\rm cc}$  and time t following a glitch. The results are calculated with PKDD with  $L_0=40$  MeV. The entrainment  $f_{\rm e}=1.0$  and NS mass  $1.4M_{\odot}$  are adopted. The gray solid line indicates the frequency of the "crust" component at t=96 s.

 $\Omega_{\rm sf}$ . We observe that the crust superfluid substantially couples with the "crust" approximately 96 seconds after the glitch, except for the weak coupling region. Smaller values of  $\mathcal{B}_{\rm crust}$  correspond to slower coupling, particularly in the weak-pinning region of the pinning configuration transition. The coupling is faster at the top of the inner crust due to the largest  $\mathcal{B}_{\rm crust}$ , although this region transfers little angular momentum according to Eq. (24) due to its small superfluid density.

The core superfluid exhibits even more dramatic dynamics, as shown in Figure 5. The strong mutual friction (high  $\mathcal{B}_{core}$ ) in the central region causes it to couple almost instantly with the crust, leading to a rapid transfer of angular momentum. This results in a clear overshoot feature, where the central superfluid's angular velocity temporarily exceeds that of the crust. Subsequently, the angular momentum of the superfluid component in the central region is transferred to other layers of the core with lower  $\mathcal{B}_{core}$ , eventually leading to the complete coupling of most of the superfluid component of the core with the crust. Since  $\mathcal{B}_{core}$  is small at the core-crust interface, the coupling of the core superfluid near the crust is slow. This region and the weak coupling region in the inner crust require more time to reach equilibrium with the "crust" component, but their impact on the observable crustal spin frequency is already minimal. We estimate that the internal equilibrium timescale  $t_{eq}$  of the NSs following the trigger of a glitch is  $\sim 100$  s.

Except for the weak coupling region in the inner crust, we have demonstrated that neither  $L_0$  nor entrainment significantly alters the distribution of the mutual friction coefficient in a given NS. The spatial and temporal

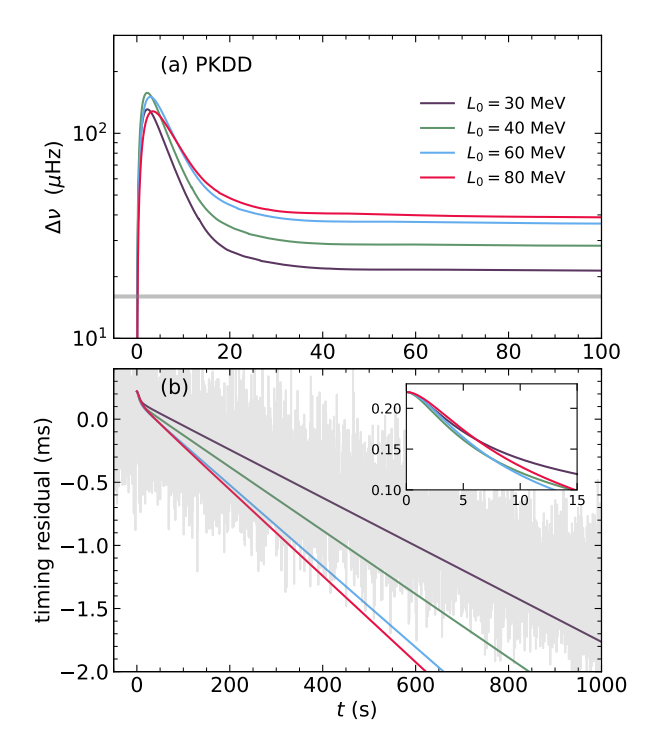


Figure 6. Glitch rise dynamics for different  $L_0$  values using the PKDD interaction. (a) Temporal evolution of the crustal frequency shift  $\Delta\nu$ , showing an overshoot whose peak and timing depend on  $L_0$ . The gray line indicates the final glitch step size  $16.02~\mu\text{Hz}$  (Palfreyman et al. 2018). (b) Corresponding model timing residuals compared to observations from Palfreyman et al. (2018) and Graber et al. (2018). The inset highlights the first 15 s, demonstrating the model's sensitivity to  $L_0$  during the initial rise.

evolutions of  $\Omega_{\rm sf}$  and  $\Omega_{\rm core}$  shown in Figures 4 and 5 exhibit qualitatively similar patterns across different effective interactions and strengths of entrainment effect. A notable difference is that, as  $L_0$  and  $f_{\rm e}$  vary, the slowly coupled region in the crust shifts in a manner consistent with the weak coupling region of  $\mathcal{B}_{\rm crust}$ . Another significant difference emerges when  $f_{\rm e}$  decreases below 0.4, the slowly coupled region vanishes along with the weak coupling region, resulting in globally faster coupling with the "crust" component.

## 3. THEORETICAL PREDICTION TO GLITCH RISE

To investigate how the EOS, entrainment effect, and NS mass influence glitch rises, we employ the three-component glitch model to simulate both the rise profiles and the corresponding model timing residuals. The observed timing residuals from Palfreyman et al. (2018), as reproduced in Graber et al. (2018), are utilized for comparison.

### 3.1. Crustal frequency evolution and model residuals

In Figure 6(a), we plot the crustal frequency  $\Delta\nu$  as a function of time t for a  $1.4M_{\odot}$  NS calculated using PKDD with different  $L_0$  in the absence of entrainment effect ( $f_{\rm e}=1.0$ ). We can clearly see that an overshoot appears just after the glitch. The overshoot of  $\Delta\nu$  acquires that the mutual friction coefficient in the crust is strong enough while that in the core is weak enough so that the angular momentum can temporarily accumulate in the "crust" component. The overshoot in  $\Delta\nu$  can be identified as the equilibrium, rise, and decay components

$$\Delta \nu = \Delta \nu_{\rm eq} + \Delta \nu_{\rm r} e^{-\frac{t}{\tau_{\rm r}}} + \Delta \nu_{\rm d} e^{-\frac{t}{\tau_{\rm d}}}, \qquad (25)$$

where  $\Delta \nu_{\rm eq}$ ,  $\Delta \nu_{\rm r}$ , and  $\Delta \nu_{\rm d}$  are the glitch step size and amplitudes of the rise and decay components.  $\tau_{\rm r}$  and  $\tau_{\rm d}$  describe the timescales of "rise" and "decay" in the frequency. Eq. (25) is similar to  $H_2$  model in Ashton et al. (2019), and  $\Delta \nu_{\rm eq} = 16.11^{+0.04}_{-0.04} \ \mu{\rm Hz}, \ \tau_{\rm r} < 12.6$  s with 90% confidence interval,  $\Delta \nu_{\rm d} = 9.36^{+12.20}_{-6.38} \ \mu{\rm Hz},$ and  $\tau_{\rm d}=65.97^{+59.38}_{-24.44}$  s are suggested. Note that  $\Delta\nu_{\rm eq}$ has been updated to  $16.01^{+0.05}_{-0.05}~\mu \text{Hz}$  in  $H_{2+p}$  model after considering the frequency slowdown preceding the glitch. By fitting Eq. (25) to the temporal evolutions of crustal frequency in Figure 6(a), we find that the glitch rise times (< 2 s) are significantly less than the observed upper limit of 12.6 s. Other parameters differ significantly from the results in Ashton et al. (2019), which arise from the different fitting procedures. We use Eq. (25) to directly fit the temporal evolutions of crustal frequency, while Ashton et al. (2019) fitted  $H_2$  model to the pulse arrival time after integrating the frequency evolution to the phase evolution.

We plot the comparison between the observed timing residual and the model timing residuals calculated by PKDD with different  $L_0$  in Figure 6(b). The model timing residual is calculated by  $-2\pi\phi/\Omega_{\rm crust}(0)$  with the phase  $\phi = \int \Delta\nu dt$ . Following Graber et al. (2018), the model timing residuals are shifted  $\Delta t = 0.22$  s at t=0 to consider the frequency slowdown preceding the glitch. We have mentioned that the superfluid becomes almost fully coupled with the "crust" component on the timescale of 100 s, so the phase can be written as

$$\phi(t) = \int_0^{t_{\rm eq}} \Delta\nu(t)dt + \Delta\nu_{\rm eq}(t - t_{\rm eq}). \tag{26}$$

The non-equilibrium state between the superfluid and "crust" components contributes the first term of the right-hand side in Eq. (26), and their equilibrium state donates the second term. Hence, the model timing residual for t>100 s is a linear function of time.  $\Delta\nu_{\rm eq}$  can be determined by angular momentum conservation,

$$\Delta \nu_{\rm eq} \approx \frac{I_{\rm sf}}{I} \frac{\Delta \Omega_{\rm crit}}{2\pi},$$
 (27)

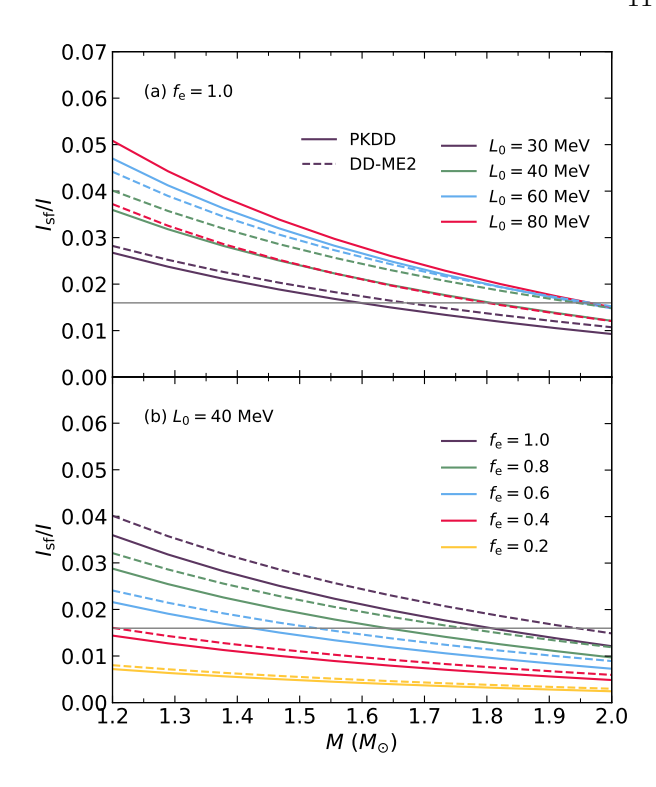


Figure 7. Fraction of the total moment of inertia carried by the crustal superfluid reservoir  $(I_{\rm sf}/I)$  as a function of NS mass. (a) Dependence on the symmetry energy slope  $L_0$  for both PKDD (solid lines) and DD-ME2 (dashed lines) interactions. The gray horizontal line marks the value required to explain the glitch step size of the 2016 Vela event. (b) Dependence on the entrainment factor  $f_{\rm e}$ , showing how stronger entrainment (lower  $f_{\rm e}$ ) systematically reduces the available angular momentum reservoir. These trends directly determine the equilibrium glitch step size  $\Delta\nu_{\rm eq}$ .

if we assume that the superfluid reservoir is completely depleted. I is total moment of inertia of NS.  $I_{\rm sf}$  is calculated by

$$I_{\rm sf} = \frac{8\pi}{3} \int_{R}^{R_{\rm oi}} r^4 \rho_s(r) \mathrm{d}r,$$
 (28)

and the total moment of inertia of NSs is given by

$$I = \frac{8\pi}{3} \int_0^R r^4 \rho(r) dr,$$
 (29)

The equilibrium frequency jump  $\Delta \nu_{\rm eq}$  is therefore closely related to these global properties of the NS, including its density distribution and the fraction of the MoI stored in the superfluid reservoir.

# 3.2. Effects of EOS, entrainment, and NS mass on the qlitch rise

Here we discuss how  $L_0$  affects the temporal evolution of the crustal frequency and the model timing residuals. In the non-equilibrium state, as we can see in Figure 6

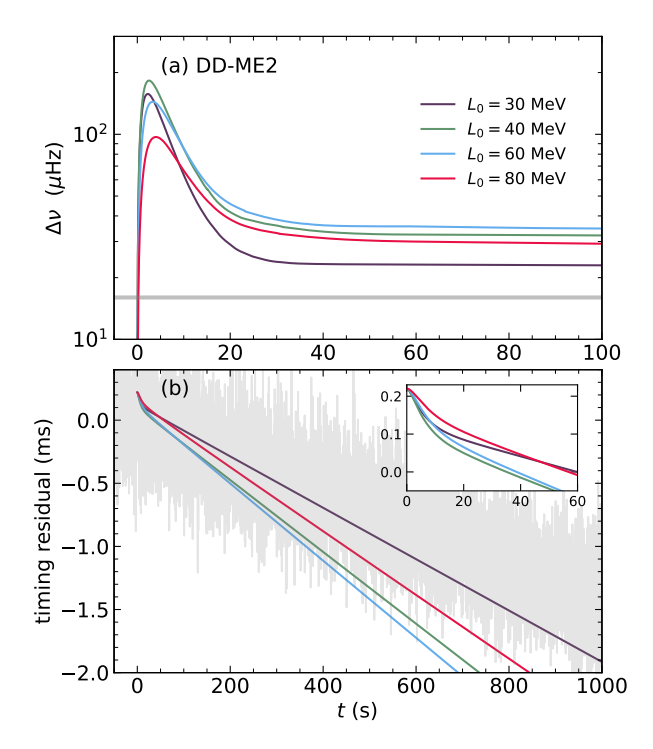


Figure 8. Glitch dynamics for the DD-ME2 interaction reveal a non-monotonic dependence on the symmetry energy slope  $L_0$ . (a) Temporal evolution of the crustal frequency shift  $\Delta\nu$  shows complex overshoot behavior that varies with  $L_0$ , in contrast to the monotonic trend seen with PKDD (Fig. 6). (b) Corresponding model timing residuals compared to observations. The inset highlights the first 60 s, where the non-monotonic dependence creates distinctive residual patterns. This contrasting behavior between nuclear interactions provides a potential discriminant for constraining the nuclear EOS.

(a), as  $L_0$  increases from 40 MeV to 80 MeV, the peak value in the overshoot decreases and the location of the peak increases. The peak is determined by the competition between the mutual friction coefficients of the crust and the core. On the one hand, larger  $L_0$  predicts a smaller  $\mathcal{B}_{\text{crust}}$  near the crust-core interface, resulting in slower glitch rise and smaller peak value; on the other hand, larger  $L_0$  also predicts a larger  $\mathcal{B}_{core}$  in the region except near the crust-core interface, leading to faster overshoot decay and smaller peak value. Consequently, as  $L_0$  increases from 40 MeV to 80 MeV, the peak value of the overshoot decreases and its corresponding time lengthens. PKDD with  $L_0 = 30$  MeV predicts nonmonotonic  $\mathcal{B}_{\text{crust}}$  near the crust-core interface, causing the shape of the overshoot to deviate from the pattern we described for  $L_0 > 40$  MeV. The complex shape of the crustal frequency in the overshoot that causes the dependence  $L_0$  of the model timing residuals is not trivial during the initial dozen seconds, as we can see in the inset of Figure 6 (b).

In the equilibrium state,  $\Delta \nu_{\rm eq}$  increases with increasing  $L_0$ , which is related to the fraction moment of inertia of crust superfluid. Eq. (28) and (29) indicates that the superfluid density  $\rho_s$ , the thickness  $d=R_{\rm oi}-R_{\rm cc}$  and radius  $R_{\rm cc}$  of the inner crust , also including the mass density  $\rho$ , affect the value of  $I_{\rm sf}/I$ . The larger  $L_0$  reduces the isospin asymmetry of nuclear matter and stiffens EOS in the median density range (Tu & Li 2025), resulting in the increase of  $\rho_s$ ,  $\rho$ , and  $R_{\rm cc}$ , and the reduction of the thickness d. Therefore, the effect of  $L_0$  on  $I_{\rm sf}/I$  is the result of competition between these four physical quantities.

The capacity for angular momentum transfer during a glitch is fundamentally set by the fractional MoI of the crustal superfluid,  $I_{\rm sf}/I$ . Figure 7 reveals how this key reservoir depends on the NS mass, the symmetry energy slope  $L_0$ , and the entrainment strength. Panel (a) shows a critical divergence between the two EOS families: while  $I_{\rm sf}/I$  increases monotonically with  $L_0$ for PKDD, it peaks at intermediate  $L_0$  (40-60 MeV) for DD-ME2. This non-monotonic behavior underscores the competing effects of  $L_0$ : it generally increases superfluid density but also thins the crust, with DD-ME2 being more sensitive to the latter. Panel (b) demonstrates that entrainment systematically suppresses  $I_{\rm sf}/I$ across all masses, directly reducing the available angular momentum reservoir and thus the predicted glitch size  $(\Delta \nu_{\rm eq})$ .

This non-monotonic dependence of the DD-ME2 interaction also leads to a non-monotonic dependence of  $\Delta\nu_{\rm eq}$  on  $L_0$ , as shown in Figure 8. It leads to a more complex correspondence between the shape of  $\Delta\nu$  and  $L_0$  in non-equilibrium states, particularly in the first 60 s (inset of panel b). Furthermore, as we will see in the next section, these two distinct  $L_0$  dependencies significantly affect the fitting results to the 2016 Vela glitch observations.

In Figure 9(a), we demonstrate how the entrainment effect affects the shape of  $\Delta\nu$  and the model timing residuals. In the non-equilibrium state, the peak of the overshoot is systematically suppressed because the mutual friction of the inner crust near the crust-core interface is systematically weakened by stronger entrainment effect, see Figure 2(b), while the mutual friction of the core remains unchanged. Consequently, the glitch rise timescale lengthens, whereas the rate of overshoot decay stays constant. In the equilibrium state,  $\Delta\nu_{\rm eq}$  decreases with enhanced entrainment, which can be simply understood as entrainment reducing the capacity of the angular momentum reservoir (i.e.,  $I_{\rm sf}/I$ , see Figure 7(b)), thereby decreasing angular momentum transfer and resulting in smaller glitch step sizes. Note that since the

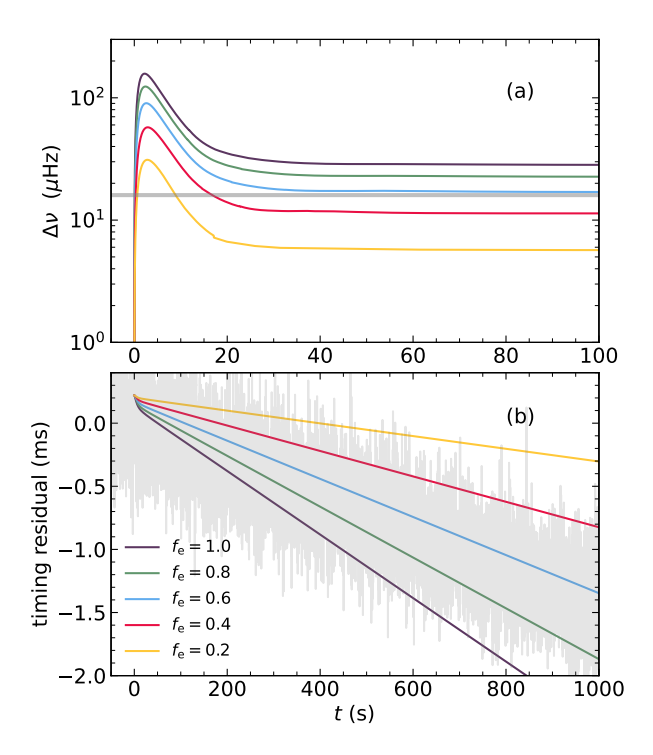


Figure 9. Systematic suppression of glitch dynamics by entrainment effects. (a) The crustal frequency shift  $\Delta\nu$  shows reduced overshoot amplitude and smaller equilibrium values with stronger entrainment (lower  $f_{\rm e}$ ). (b) Model timing residuals demonstrate high sensitivity to the entrainment factor  $f_{\rm e}$ , particularly in the initial 15 s (inset). This sensitivity provides a direct observational constraint on the fraction of free neutrons participating in superflow, with our analysis favoring weak entrainment ( $f_{\rm e} \gtrsim 0.7$ ).

overshoot needs to decay to different  $\Delta\nu_{\rm eq}$  values depending on  $L_0$ , the decay timescale is not constant. As depicted in Figure 9(b), the model timing residuals are highly sensitive to the entrainment effect, providing a potential method to constrain the strength of the entrainment effects in NS interiors.

In Figure 10 (a), we show how the NS mass affects the shape of  $\Delta\nu$  and the model timing residuals. In the non-equilibrium state, the peak of the overshoot is systematically suppressed because the core region with strong mutual friction expands as the NS mass increases, meanwhile the thickness of the inner crust becomes thinner. Consequently, the overshoot decay timescale shortens, whereas the rate of glitch rise remains unchanged. In the equilibrium state,  $\Delta\nu_{\rm eq}$  decreases with NS mass, which can be simply understood as the capacity of the angular momentum reservoir (i.e.,  $I_{\rm sf}/I$ , see Figure 7) is reduced due to the thinner inner crust, thereby decreasing angular momentum transfer and resulting in smaller glitch step sizes. As depicted in Figure 10(b), the model timing residuals are highly sensitive to the NS mass, pro-

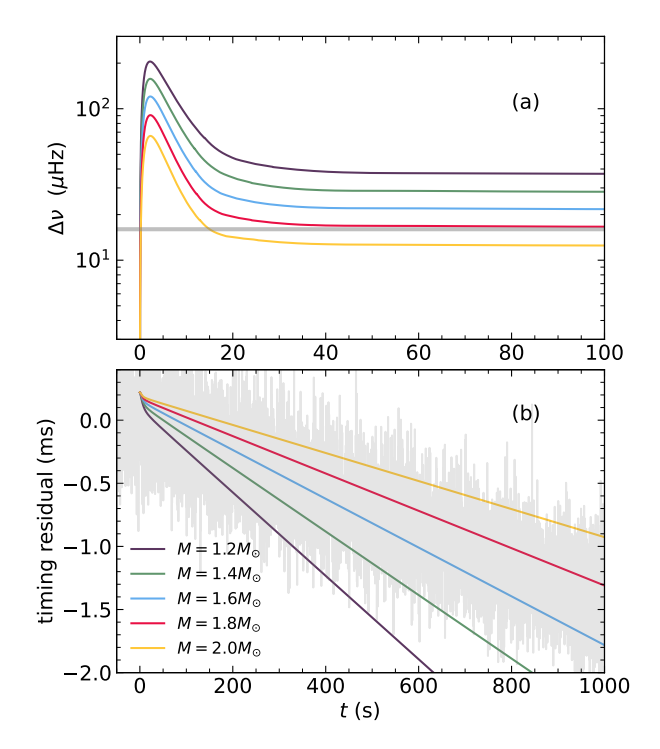


Figure 10. NS mass as a determining factor in glitch characteristics. (a) Higher mass NSs exhibit suppressed overshoot and smaller glitch steps due to reduced crustal moment of inertia. (b) The corresponding timing residuals show distinct mass-dependent signatures, particularly in the overshoot region. This mass sensitivity enables glitch observations to serve as a weighing tool for pulsars, with the 2016 Vela glitch constraining its mass to 1.05–1.65  $M_{\odot}$ .

viding a potential method to measure the NS mass by the timing observation of the pulsar.

### 4. MODEL FITTING TO THE 2016 VELA GLITCH

We have confirmed that the entrainment effect, the NS mass, and EOSs significantly affect the glitch rises. In the next section, we try to constrain these factors by using the three-component glitch model with the unified EOS and the self-consistent calculated  $\mathcal{B}_{\text{crust}}$ .

### 4.1. MCMC simulations and parameter correlations

To determine the parameters of the three-component glitch model by fitting the 2016 Vela glitch, we first extended the model to incorporate the observed preglitch crustal slowdown, denoted as  $\Delta\nu_{-}$ . In Ashton et al. (2019), this pre-glitch frequency decrease was estimated as  $\Delta\nu_{-}=5.40^{+3.39}_{-2.05}~\mu{\rm Hz}$  over a duration of approximately 100 s, modeled using a simple rectangular function. The authors suggested that this transient slowdown could represent a stochastic fluctuation that triggered the glitch by increasing the rotational lag between the crust and the superfluid beyond its critical threshold. Gügercinoğlu & Alpar (2020) proposed that

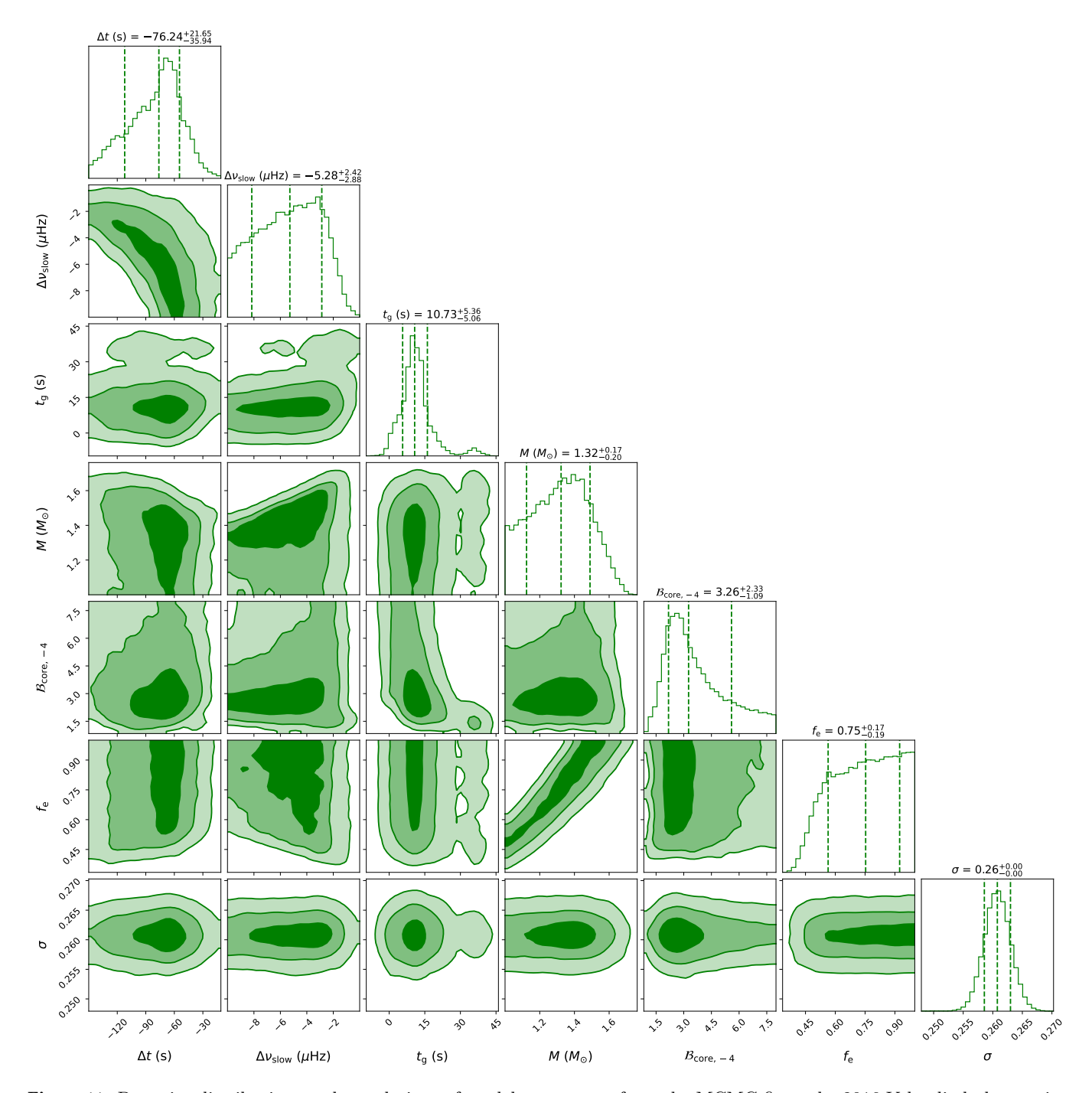


Figure 11. Posterior distributions and correlations of model parameters from the MCMC fit to the 2016 Vela glitch data, using the PKDD interaction with  $L_0 = 40$  MeV. The anti-correlation between the pre-glitch slowdown duration  $\Delta t$  and magnitude  $\Delta \nu_{\rm slow}$ , and the positive correlation between NS mass M and entrainment factor  $f_{\rm e}$ , are clearly visible. ( $\mathcal{B}_{\rm core, -4} = \mathcal{B}_{\rm core}/10^{-4}$ ).

the slowdown event signal the formation of a new vortex trap zone by a crust breaking quake, and initiates the large-scale vortex unpinning avalanche and induces short-lived magnetospheric changes. In this work, we follow the treatment in Ashton et al. (2019) by phenomenologically modeling the slowdown in the crustal frequency using a rectangular function, where the triggering of the glitch immediately follows the slowdown event. The complete model is therefore expressed as:

$$\Delta\nu(t) = \Delta\nu_{\text{slow}}\Pi(t; t_{\text{g}} + \Delta t, t_{\text{g}}^{-}) + (\Delta\nu_{3c} - \Delta\nu_{\text{slow}})H(t - t_{\text{g}}),$$
(30)

where  $t_{\rm g}$  is the glitch time,  $\Pi$  is the rectangle function such that the frequency decreases by  $\Delta\nu_{\rm slow}$  for the period  $|\Delta t|$  prior the glitch. Note that in our simulations the crustal frequency does not recover to its pre-slowdown value.  $\Delta \nu_{\rm sc}$  represents the postglitch frequency evolution calculated through the threecomponent model.  $H(t-t_g)$  is the Heaviside step function. In the three-component glitch model, we treat  $\mathcal{B}_{\text{core}}$  as a free parameter to investigate the mechanism of the core mutual friction. Since our unified EOSs and the self-consistent mutual friction coefficients are calculated with several effective interactions spanning both the isoscalar and isovector channels, the fittings are performed across all effective interactions. There are six model parameters to be determined in our model:  $\Delta t$ ,  $\Delta \nu_{\text{slow}}, t_{\text{g}}, M, \mathcal{B}_{\text{core}}, \text{ and } f_{\text{e}}.$ 

We investigated the rise phase of the 2016 Vela glitch by implementing Eq. (30) within a MCMC framework, employing the emcee ensemble sampler to perform robust parameter estimation. The model  $\Delta \nu(t)$  is integrated to generate the model timing residuals r(t) = $-2\pi\phi(t)/\Omega_{\rm crust}$ , which are subsequently fitted against the observed timing residuals. The priors of  $\Delta t$ ,  $\Delta \nu_{\rm slow}$ , and  $t_{\rm g}$  are selected as uniform distributions based on the estimation of the previous work (Ashton et al. 2019):  $\Delta t(s) \sim \text{Uniform}[-100, -10], \ \Delta \nu_{\text{slow}}(\mu \text{Hz}) \sim$ Uniform[-10,0], and  $t_g(s) \sim \text{Uniform}[-10,50]$ . The prior of NS mass M is the uniform distribution based on the observed upper limit (Romani et al. 2022):  $M(M_{\odot}) \sim \text{Uniform}[1.0, 2.3].$  For the prior of  $\mathcal{B}_{\text{core}}$ , the preliminary fits indicated  $\mathcal{B}_{core}$  was consistently  $\sim 10^{-4}$ , so we set a uniform prior around this value:  $\mathcal{B}_{\text{core},-4} \sim \text{Uniform}[1.0, 8.0], \, \mathcal{B}_{\text{core},-4} = \mathcal{B}_{\text{core}}/10^{-4}.$  For the strength of the entrainment effect, we adopt a uniform prior distribution  $f_e \sim \text{Uniform}[0.05, 1.00]$ , where the lower limit approaches the theoretical value of 0.08 from Chamel (2024), and the upper limit corresponds to the case without the entrainment effect. An additional free parameter is the uncertainty  $\sigma$  on single measurement of the time residual. Assuming that the influence

of  $\sigma$  on the correlation between timing residuals and pulse arrival times is negligible, we adopt a uniform prior  $\sigma \sim \text{Uniform}[0.2,0.3]$ . Given the definition of  $\sigma$ , and under the assumption that individual pulse measurements are statistically independent, the likelihood function can be expressed following Ashton et al. (2019); Montoli, A. et al. (2020) as:

$$\mathcal{P} \sim \prod_{i} \frac{1}{\sqrt{2\pi\sigma^2}} e^{-\frac{(r(t_i) - r_i)^2}{2\sigma^2}},$$
 (31)

where  $r_i$  is the single measured timing residual. We focus primarily on the model fitting for glitch rise and overshoot of crustal frequency, thus truncating the time window to 600 s symmetrically centered on the dataset. Fitting results using the full dataset do not qualitatively alter our conclusions.

We display the posterior distributions of the model parameters and the uncertainty  $\sigma$  for the glitch rise simulation of the 2016 Vela glitch in Figure 11. We can find that significant correlations exist only between parameter pairs, i.e.,  $(\Delta t, \Delta \nu_{\text{slow}})$  and  $(M, f_{\text{e}})$ . The anti-correlation between  $\Delta t$  and  $\Delta \nu_{\rm slow}$  remains consistent with Ashton et al. (2019). The two parameters are introduced to fit the elevated timing residuals caused by the slowdown prior to the glitch, and both  $\Delta t$  and  $\Delta \nu_{\rm slow}$  contribute positively to the amplitude of the timing residual. Therefore, an increase in one parameter necessarily requires a decrease in the other. The positive correlation between M and  $f_e$  is also clearly demonstrated in Figure 7, revealing that the Vela mass is required to decrease with stronger entrainment to match the observed glitch step size. This correlation arises because entrainment reduces the capacity of the angular momentum reservoir, consequently decreasing the available angular momentum transfer to support the glitch. In Tu & Li (2025), the snowplow model was applied to the 2000 Vela glitch, revealing a positive correlation between the Vela mass and the pinning force strength. As shown in Figure 1, entrainment acts as a suppressing mechanism for pinning. This implies that the positive correlation between the Vela mass and  $f_e$  likewise applies within the framework of the snowplow model for the 2000 Vela glitch.

### 4.2. Constraints on the Vela's mass, EOS, and interiors

In Table 4, we collect the marginalized posterior of model parameters in all cases of effective interactions. Although  $\Delta t$ ,  $\Delta \nu_{\rm slow}$ , and  $t_{\rm g}$  do not involve EOS, they are affected by the overall fitting. It is clear that  $\Delta t$  exhibits a decreasing trend with  $L_0$ , while  $\Delta \nu_{\rm slow}$  shows a corresponding increasing trend due to their intrinsic

 $\mathcal{B}_{\text{core},-4}$ 

 $f_{\rm e}$ 

	DD-ME2				PKDD				
$L_0 \text{ (MeV)}$	30	40	60	80	30	40	60	80	
$\Delta t$ (s)	$-78.10^{+23.72}_{-35.69}$	$-74.42^{+23.28}_{-35.90}$	$-75.60^{+22.29}_{-36.91}$	$-75.23^{+22.51}_{-36.96}$	$-76.69^{+22.76}_{-35.40}$	$-76.24^{+21.65}_{-35.94}$	$-75.02^{+21.86}_{-35.02}$	$-74.42^{+21.66}_{-33.97}$	
$\Delta \nu_{\rm slow} \ (\mu {\rm Hz})$		$-5.51^{+2.53}_{-2.91}$	$-5.47^{+2.52}_{-2.91}$	$-5.48^{+2.50}_{-2.90}$	$-5.04^{+2.26}_{-3.05}$	$-5.28^{+2.42}_{-2.88}$	$-5.50^{+2.46}_{-2.88}$	$-5.62^{+2.52}_{-2.83}$	
$t_{\rm g}$ (s)	$11.00^{+5.76}_{-5.36}$	$10.26^{+5.34}_{-5.61}$	$9.20^{+5.93}_{-5.63}$	$8.85^{+5.89}_{-5.82}$	$10.86^{+6.73}_{-5.26}$	$10.73^{+5.36}_{-5.06}$	$9.37^{+5.46}_{-5.64}$	$8.67^{+5.72}_{-5.91}$	
$M~(M_{\odot})$	$1.21^{+0.14}_{-0.14}$	$1.39^{+0.20}_{-0.24}$	$1.43^{+0.19}_{-0.25}$	$1.34^{+0.15}_{-0.20}$	$1.18^{+0.14}_{-0.12}$	$1.32^{+0.17}_{-0.20}$	$1.42^{+0.20}_{-0.25}$	$1.46^{+0.20}_{-0.27}$	

 $2.90^{+2.35}_{-1.04}$ 

 $0.75^{+0.17}_{-0.20}$ 

 $0.83^{+0.12}_{-0.14}$ 

Table 4. Marginalized posterior of model parameters fitted to the 2016 Vela glitch for DD-ME2 and PKDD with varying values of  $L_0$ . The values are given by  $1\sigma$  errors.

correlation. The trigger time of the glitch exhibits an anti-correlation with  $L_0$ , indicating that the inferred  $t_g$  from observations can serve as an additional probe for constraining the EOS.

 $0.73^{+0.19}_{-0.20}$ 

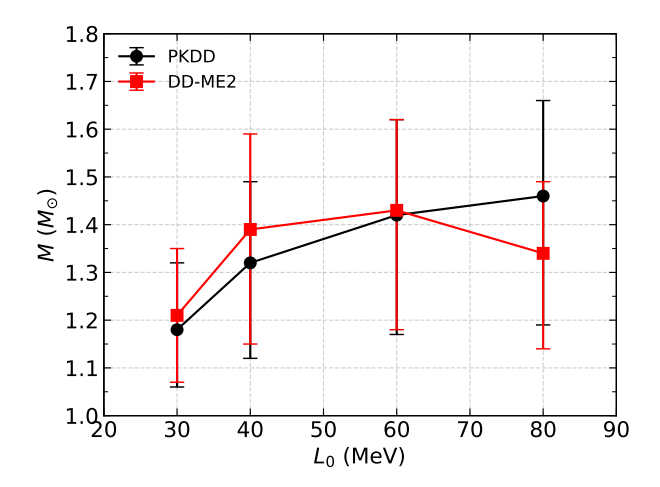
 $0.71^{+0.19}_{-0.21}$ 

 $0.81^{+0.13}_{-0.13}$ 

The Vela mass exhibits distinct  $L_0$ -dependencies under two set of effective interactions, consistent with the trends shown in Figure 7. These dependencies are further visualized in Figure 12. For PKDD, the Vela mass increases monotonically with  $L_0$ , though the rate of increase diminishes at higher values of  $L_0$ . However, DD-ME2 produces a non-monotonic correlation in which the Vela mass first rises and then falls with increasing  $L_0$ , with a potential peak occurring between 40–60 MeV. The divergent  $L_0$ -dependence of the Vela mass for DD-ME2 and PKDD may correlate with several low-order isoscalar parameters of nuclear matter, such as the incompressibility  $K_0$ , potentially linking to properties of finite nuclei and heavy-ion collisions.

Combining the results from all EOS variants, we constrain the mass of the Vela pulsar to the range of  $1.05\text{--}1.65~M_{\odot}$ . This is broadly consistent with the constraint of  $1.25\text{--}1.45~M_{\odot}$  from the maximum glitch size (Pizzochero et al. 2017) and is close to the lower limit inferred from the 2000 glitch by Shang & Li (2021). However, it is in tension with the high-mass solution (>2.0  $M_{\odot}$ ) found by Tu & Li (2025) for the 2000 glitch using the snowplow model, highlighting how different glitch models and observed events can lead to divergent inferences.

For both DD-ME2 and PKDD, the core mutual friction coefficient  $\mathcal{B}_{core}$  first increases and then decreases with the symmetry energy slope  $L_0$ . The overall variation remains small, indicating that  $\mathcal{B}_{core}$  is only weakly sensitive to the EOS. With  $\mathcal{B}_{core}$  consistently around the order of  $10^{-4}$ , it is unlikely that the dominant contribution to core mutual friction arises from Kelvin-wave excitations induced by vortex–fluxtube interactions. It should be noted that Eq. (21) describing  $\mathcal{B}$ core is applicable to the outer core region, where the density is



 $0.75^{+0.17}_{-0.19}$ 

 $3.25^{+2.32}_{-1.16}$ 

 $0.67^{+0.21}_{-0.22}$ 

 $0.68^{+0.22}_{-0.02}$ 

Figure 12. The Vela masses with  $1\sigma$  errors, which inferred from MCMC simulations, as a function of  $L_0$  for DD-ME2 and PKDD.

typically  $\rho \sim 10^{14}~{\rm g\,cm^{-3}}$  and the proton fraction is  $Y \rm p \sim 0.05$ . Since the NS mass inferred from our fitting is relatively low, the corresponding core densities do not deviate significantly from this validity range. Therefore, the primary mechanism of core mutual friction is most likely the scattering of electrons off magnetized vortices rather than vortex–fluxtube coupling.

For both EOS parameterizations, the entrainment effect first strengthens and then weakens with  $L_0$ , but the trend is even less obvious for PKDD due to the correction between the Vela mass and  $f_{\rm e}$ . The weak entrainment effect inferred from our study qualitatively supports the theoretical calculation in Almirante & Urban (2025).

### 5. SUMMARY AND PERSPECTIVE

In this study, we have used the superfluid coupling dynamics during the 2016 Vela glitch to probe the dense matter EOS, the mass of the Vela pulsar, and the properties of its interior. For the purpose, we refitted DD-ME2 and PKDD to nuclear saturation properties and applied them to construct several unified EOSs, enabling self-

consistent calculations of the interior composition, superfluidity, and global properties of NSs. Building upon this foundation, we further self-consistently calculated the mutual friction coefficients  $\mathcal{B}_{crust}$  in the inner crust based on Kelvin-wave excitation between vortices and nuclear clusters, while the mutual friction coefficients  $\mathcal{B}_{\text{core}}$  in the core are derived by assuming the electron scattering off magnetized vortices as the dominant mechanism. By developing the three-component glitch model to incorporate the differential rotation of the core superfluid, we systematically analyzed the complex superfluid coupling dynamics across different regions within a typical NS and investigated how three key parameters, i.e.,  $L_0$ ,  $f_e$ , and NS mass, affect the glitch rise and the overshoot in the crustal frequency. Through fitting timing observations of the 2016 Vela glitch, we established constraints on these parameters.

We find that the density dependence of the mutual friction coefficient leads to complex coupling dynamics within the NSs. Specifically, the stronger mutual friction coefficient in the central region of the NSs produces an overshoot feature there. The overshoot in the crustal frequency is jointly determined by both the crustal and core mutual friction coefficients. Except for the case of  $L_0 = 30 \text{ MeV}$ , increasing  $L_0$  systematically reduces the crustal mutual friction coefficient near the crust-core interface but enhances it in the core regions farther away, resulting in a decrease in the peak of the overshoot. The  $L_0$ -dependence of the capacity of the angular momentum reservoir depends on the EOSs, leading to two distinct patterns for the correlation between the predicted glitch step size and  $L_0$ : monotonic increase (PKDD) and increase-then-decrease (DD-ME2). A stronger entrainment effect reduces both the crustal mutual friction coefficient and the capacity of the angular momentum reservoir, causing both a lower peak of the overshoot and a smaller glitch step size. The larger NS mass corresponds to reduced capacity of the angular momentum reservoir, resulting in a lower peak of the overshoot and a smaller glitch step size.

We performed MCMC simulations of the timing residuals of the 2016 Vela glitch using the three-component glitch model. The inferred value of  $\mathcal{B}$ core is on the order of  $10^{-4}$ , which essentially rules out the possibility of Kelvin wave excitation between the vortex and fluxtube as the dominant friction mechanism. Within the inner crust, the entrainment effect is found to be relatively weak, with a median estimate indicating that approximately 70% of the free neutrons remain effectively superfluid.

Our analysis further reveals a general anti-correlation between the Vela mass and the strength of the en-

The dependence of Vela mass on trainment effect.  $L_0$  exhibits two distinct patterns: monotonic increase (PKDD) and increase-then-decrease (DD-ME2), which depends on the effective interaction in the isoscalar channel. Combining these results, we constrain the Vela pulsar mass to the range  $1.05-1.65 M_{\odot}$ . Previously, using the same effective interactions and self-consistently calculated crustal pinning forces as our study, Tu & Li (2025) applied the snowplow model to fit the 2000 Vela glitch observations and suggested that Vela is a massive NS ( $>2.0M_{\odot}$ ) for Vela. However, this inferred mass is significantly higher than the upper limit obtained in our analysis. The discrepancy between the two studies may arise from several key differences: (1) Tu & Li (2025) did not include the entrainment effect, which can substantially reduce the effective superfluid moment of inertia; (2) the snowplow model considers only the unpinning of a fraction of vortices and a limited portion of the inner crust's moment of inertia, while our treatment includes a more complete coupling of components; (3) the two glitches may have been triggered by distinct physical mechanisms—for instance, the 2016 Vela glitch analyzed here may have been initiated by a crustal fracture (starquake); and (4) Tu & Li (2025) constrained the model parameters by fitting the step changes in spin frequency and its derivative about one minute after the glitch, whereas our analysis focuses on the detailed timing residuals within a truncated 600-second post-glitch window, capturing the early relaxation dynamics. Future high-cadence, high-precision timing observations with facilities such as FAST, SKA, and eXTP will be essential for resolving glitch rise times and transient overshoots with millisecond accuracy, thereby enabling more stringent tests of competing models.

Finally, while glitches are generally interpreted as sudden angular momentum transfer from a pinned superfluid reservoir to the crust, the opposite phenomenon—anti-glitches—has also been reported, most prominently in magnetars and tentatively in several rotation-powered pulsars. Within a dynamical framework, anti-glitches correspond to a net loss of crustal angular momentum relative to the superfluid. From the perspective of frictional coupling, both glitches and anti-glitches probe the same underlying physics, but in different regimes: glitches constrain the efficiency and timescale of vortex unpinning and outward angular momentum transfer, whereas anti-glitches reveal conditions under which angular momentum is withheld from the crust or external braking is enhanced. Studying glitches and anti-glitches within a unified dynamical framework therefore expands the accessible parameter space of superfluid friction and provides complementary sensitivity

to the EOS, especially when combined with coordinated multi-wavelength monitoring.

### ACKNOWLEDGMENTS

The work is supported by the National SKA Program of China (No. 2020SKA0120300), the National Natural Science Foundation of China (grant Nos. 12273028, 12494572).

#### REFERENCES

- Almirante, G., & Urban, M. 2025. https://arxiv.org/abs/2503.21635
- Alpar, M. A. 1977, Astrophys. J, 213, 527, doi: 10.1086/155183
- Alpar, M. A., Chau, H. F., Cheng, K. S., & Pines, D. 1993, Astrophys. J, 409, 345, doi: 10.1086/172668
- —. 1996, Astrophys. J, 459, 706, doi: 10.1086/176935
- Alpar, M. A., Cheng, K. S., & Pines, D. 1989, Astrophys. J, 346, 823, doi: 10.1086/168063
- Alpar, M. A., Pines, D., Anderson, P. W., & Shaham, J. 1984, Astrophys. J, 276, 325, doi: 10.1086/161616
- Anderson, P. W., & Itoh, N. 1975, Nature, 256, 25, doi: 10.1038/256025a0
- Andersson, N., Glampedakis, K., Ho, W. C. G., & Espinoza, C. M. 2012, Phys. Rev. Lett., 109, 241103, doi: 10.1103/PhysRevLett.109.241103
- Andersson, N., Sidery, T., & Comer, G. L. 2006, Mon. Not.R. Astron. Soc, 368, 162,doi: 10.1111/j.1365-2966.2006.10147.x
- Antonopoulou, D., Haskell, B., & Espinoza, C. M. 2022,Rep. Prog. Phys, 85, 126901,doi: 10.1088/1361-6633/ac9ced
- Ashton, G., Lasky, P. D., Graber, V., & Palfreyman, J. 2019, Nature Astronomy, 36, 844, doi: 10.1038/s41550-019-0844-6
- Baym, G., Pethick, C., Pines, D., & Ruderman, M. 1969, Nature, 224, 872, doi: 10.1038/224872a0
- Bransgrove, A., Beloborodov, A. M., & Levin, Y. 2020, Astrophys. J, 897, 173, doi: 10.3847/1538-4357/ab93b7
- Carter, B., Chamel, N., & Haensel, P. 2005, Nuclear Physics A, 748, 675, doi: 10.1016/j.nuclphysa.2004.11.006
- Chamel, N. 2005, Nucl. Phys. A, 747, 109,
  doi: https://doi.org/10.1016/j.nuclphysa.2004.09.011
  —. 2024. https://arxiv.org/abs/2412.05599
- Dodson, R. G., McCulloch, P. M., & Lewis, D. R. 2002, Astrophys. J, 564, L85–L88, doi: 10.1086/339068
- Epstein, R. I., & Baym, G. 1992, Astrophys. J, 387, 276, doi: 10.1086/171079
- Espinoza, C. M., Lyne, A. G., Stappers, B. W., & Kramer, M. 2011, Mon. Not. R. Astron. Soc, 414, 1679, doi: 10.1111/j.1365-2966.2011.18503.x

- Fantina, A. F., Chamel, N., Pearson, J. M., & Goriely, S. 2013, A&A, 559, A128, doi: 10.1051/0004-6361/201321884
- Fetter, A. L., Walecka, J. D., & Kadanoff, L. P. 1972, Physics Today, 25, 54, doi: 10.1063/1.3071096
- Glampedakis, K., Andersson, N., & Samuelsson, L. 2011, MNRAS, 410, 805, doi: 10.1111/j.1365-2966.2010.17484.x
- Graber, V., Andersson, N., & Hogg, M. 2017, International Journal of Modern Physics D, 26, 1730015, doi: 10.1142/S0218271817300154
- Graber, V., Cumming, A., & Andersson, N. 2018, Astrophys. J, 865, 23, doi: 10.3847/1538-4357/aad776
- Grover, H., Gügercinoğlu, E., Joshi, B. C., et al. 2025. https://arxiv.org/abs/2506.02100
- Gügercinoğlu, E. 2017, J. Phys: Conf. Ser., 932, 012037, doi: 10.1088/1742-6596/932/1/012037
- Gügercinoğlu, E., & Alpar, M. A. 2020, Mon. Not. R. Astron. Soc, 496, 2506, doi: 10.1093/mnras/staa1672
- Haskell, B., & Melatos, A. 2015, Inter. Jour. Mod. Phys. D, 24, 1530008, doi: 10.1142/s0218271815300086
- Hooker, J., Newton, W. G., & Li, B.-A. 2013, Jour. Phys. Conf. Ser, 420, 012153,doi: 10.1088/1742-6596/420/1/012153
- Kashiwaba, Y., & Nakatsukasa, T. 2019, Phys. Rev. C, 100, 035804, doi: 10.1103/physrevc.100.035804
- Lalazissis, G. A., Niksić, T., Vretenar, D., & Ring, P. 2005, Phys. Rev. C, 71, 024312, doi: 10.1103/PhysRevC.71.024312
- Li, A., Dong, J. M., Wang, J. B., & Xu, R. X. 2016, Astrophys. J. Suppl. Ser., 223, 16, doi: 10.3847/0067-0049/223/1/16
- Li, A., & Wang, R. 2017, Proc. Int. Astron. Union, 13, 360, doi: 10.1017/S174392131700727X
- Link, B. 2003, Phys. Rev. Lett., 91, 101101, doi: 10.1103/PhysRevLett.91.101101
- —. 2014, Astrophys. J, 789, 141,doi: 10.1088/0004-637x/789/2/141
- Long, W., Meng, J., Giai, N. V., & Zhou, S.-G. 2004, Phys. Rev. C, 69, 034319, doi: 10.1103/PhysRevC.69.034319
- Montoli, A., Antonelli, M., Magistrelli, F., & Pizzochero, P. M. 2020, A&A, 642, A223, doi: 10.1051/0004-6361/202038340

- Oyamatsu, K., & Yamada, M. 1994, Nuclear Physics A, 578, 181, doi: 10.1016/0375-9474(94)90975-x
- Palfreyman, J., Dickey, J. M., Hotan, A., Ellingsen, S., & van Straten, W. 2018, Nature, 556, 219, doi: 10.1038/s41586-018-0001-x
- Pizzochero, P. M., Antonelli, M., Haskell, B., & Seveso, S. 2017, Nat. Astron, 1, 0134, doi: 10.1038/s41550-017-0134
- Pizzochero, P. M., Montoli, A., & Antonelli, M. 2020, A&A, 636, A101, doi: 10.1051/0004-6361/201937019
- Radhakrishnan, V., & Manchester, R. N. 1969, Nature, 222, 228, doi: 10.1038/222228a0
- Reichley, P. E., & Downs, G. S. 1969, Nature, 222, 229, doi: 10.1038/222229a0
- Romani, R. W., Kandel, D., Filippenko, A. V., Brink, T. G., & Zheng, W. 2022, Astrophys. J. Lett, doi: 10.3847/2041-8213/ac8007
- Serot, B. D. 1992, Rep. Prog. Phys, 55, 1855, doi: 10.1088/0034-4885/55/11/001
- Seveso, S., Pizzochero, P. M., Grill, F., & Haskell, B. 2016, Mon. Not. R. Astron. Soc, 455, 3952, doi: 10.1093/mnras/stv2579

- Shang, X., & Li, A. 2021, Astrophys. J, 923, 108, doi: 10.3847/1538-4357/ac2e94
- Sidery, T., & Alpar, M. A. 2009, Monthly Notices of the Royal Astronomical Society, 400, 1859, doi: 10.1111/j.1365-2966.2009.15575.x
- Tian, Y., Ma, Z. Y., & Ring, P. 2009, Phys. Lett. B, 676, 44, doi: 10.1016/j.physletb.2009.04.067
- Tu, Z., & Li, A. 2025, Astrophys. J, 984, 200, doi: 10.3847/1538-4357/adc80e
- Tu, Z., Sun, X., Han, S., Miao, Z., & Li, A. 2025, Phys. Rev. D, 112, 043018, doi: 10.1103/bmb3-ktz6
- Walecka, J. 1974, Ann. Phys, 83, 491, doi: 10.1016/0003-4916(74)90208-5
- Watanabe, G., & Pethick, C. J. 2017, Phys. Rev. Lett., 119, 062701, doi: 10.1103/PhysRevLett.119.062701
- Yan, Y. 2019, Res. Astron. Astrophys, 19, 072, doi: 10.1088/1674-4527/19/5/72